

1 **itle: Effective flow properties of heterolithic, cross-bedded**
2 **tidal sandstones: Part 1. Surface-based modeling**

3

4 Authors: **BENOÎT Y. G. MASSART^{1,2*}**, **MATTHEW D. JACKSON¹**, **GARY J. HAMPSON¹**,
5 **HOWARD D. JOHNSON¹**, **BERIT LEGLER^{1,3}**, **CHRISTOPHER A.-L. JACKSON¹**

6 ¹ Department of Earth Science and Engineering, Imperial College London, South Kensington
7 Campus, London SW7 2AZ, UK.

8 ² Current address: Statoil ASA, Sandsliveien 90, Bergen 5254, Norway.

9 ³ Current address: Wintershall, 34119 Kassel, Germany.

10 *E-mail of corresponding author: bmass@statoil.com

11

12 **Acknowledgements**

13 Funding for this work and approval for publication is gratefully acknowledged from
14 Norske Shell, Statoil, Total and Petoro. We thank Roxar for providing academic licenses for
15 RMS® software with which models were gridded and visualized, and Schlumberger for
16 providing academic licenses for Petrel® and ECLIPSE 100 software. The authors would like to
17 thank Rodmar Ravnås and Marcus Sarginson (Norske Shell) for advice and guidance in the
18 research project, as well as M.Sc. students Ayana Bréhéret and Justine Daboer (Imperial
19 College London). We gratefully acknowledge C. Hern, M. Sweet, F. Whitehurst and an
20 anonymous reviewer for their constructive reviews and editorial comments.

21

22 **Abstract**

23 Tidal heterolithic sandstones are often characterized by millimeter- to centimeter-scale
24 intercalations of mudstone and sandstone. Consequently, their effective flow properties are
25 poorly predicted by (1) data that do not sample a representative volume, or (2) models that
26 fail to capture the complex three-dimensional architecture of sandstone and mudstone

27 layers. We present a modelling approach in which surfaces are used to represent all
28 geologic heterogeneities that control the spatial distribution of reservoir rock properties
29 (“surface-based modeling”). The workflow uses template surfaces to represent
30 heterogeneities classified by geometry rather than length-scale. The topology of the
31 template surfaces is described mathematically by a small number of geometric input
32 parameters and models are constructed stochastically. The methodology has been applied
33 to generate generic, 3D mini-models (9 m³ volume) of cross-bedded heterolithic sandstones
34 representing trough and tabular cross-bedding with differing proportions of sandstone and
35 mudstone, using conditioning data from two outcrop analogs from a tide-dominated deltaic
36 deposit. The mini-models capture the cross-stratified architectures observed in outcrop and
37 are suitable for flow simulation, allowing computation of effective permeability values for
38 use in larger-scale models. We show that mudstone drapes in cross-bedded heterolithic
39 sandstones significantly reduce effective permeability and also impart permeability
40 anisotropy in the horizontal as well as vertical flow directions. The workflow can be used
41 with subsurface data, supplemented by outcrop analog observations, to generate effective
42 permeability values to be derived for use in larger-scale reservoir models. The methodology
43 could be applied to the characterization and modeling of heterogeneities in other types of
44 sandstone reservoirs.

45

46 **Introduction**

47 Heterolithic sandstones are commonly generated by tidal processes in shallow marine
48 environments, such as deltaic and estuarine depositional systems. In these tidally-influenced
49 environments, the main current direction varies depending on the relative strength of tidal

50 currents over daily to twice-daily cyclical time periods, and the interaction of tidal currents
51 with waves and river currents (e.g. Dalrymple and Choi, 2007). Sand is transported as
52 bedload by strong currents to form ripples and dunes during periods of rising (flood) and
53 falling (ebb) tide, and mudstone drapes are deposited during intervening slack-water
54 periods. Depending on the flow regime, the mudstone drapes are more or less continuous
55 over the sandy bedforms (Reineck and Wunderlich, 1968; Reineck and Singh, 1980; Nio and
56 Yang, 1991). This results in interstratified, millimeter- to centimeter-thick sandstone and
57 mudstone layers that are deposited over multiple tidal cycles, and form the fine-scale
58 heterogeneities that are characteristic of heterolithic tidal sandstone reservoirs. The
59 distribution of mudstones and sandstones is delimited by a hierarchy of stratigraphic
60 surfaces including (in order of increasing length scale): (1) lamina boundaries and
61 reactivation surfaces that record incremental migration of bedforms, (2) the erosional bases
62 of beds and bedsets, (3) boundaries between facies and facies associations, and (4)
63 sequence stratigraphic surfaces. These four levels of stratigraphic surfaces define the multi-
64 scale architecture and connectivity of mudstone and sandstone layers which, in turn, exerts
65 a key control on the flow of gas, oil and water during field production (Weber, 1986; Jackson
66 *et al.*, 2003, 2005; Ringrose *et al.*, 2005; Nordahl *et al.*, 2005, 2006; Nordahl and Ringrose,
67 2008).

68 The presence of these multi-scale heterogeneities in heterolithic tidal sandstone
69 reservoirs ensures that the characterization of effective reservoir properties such as
70 permeability, relative permeability, and capillary pressure, is a recurring problem (e.g.
71 Martinius *et al.*, 2005). Effective reservoir properties are typically derived from subsurface
72 well data such as wireline logs and well tests, combined with laboratory measurements on
73 cores and core plugs. Laboratory-derived reservoir properties are measured at a length scale

74 that is small (of the order centimeters for a typical core plug) compared to the dimensions of
75 grid cells in reservoir simulation models (of the order tens to hundreds of meters in plan-
76 view, and 10's cm to meters in the vertical direction). In the case of tidal heterolithic
77 sandstones, lateral and vertical variations in the continuity and connectivity of sandstone
78 and mudstone laminae (e.g. meters to tens of meters) are not sampled by either subsurface
79 well data or laboratory measurements. However, effective reservoir properties in
80 heterolithic units are highly dependent on the volume sampled (Norris and Lewis, 1991;
81 Jackson *et al.*, 2003, 2005; Nordahl and Ringrose, 2008). Consequently, effective reservoir
82 properties derived solely from subsurface and laboratory data in such heterolithic units are
83 not representative of reservoir behavior; instead, models are required that capture the
84 continuity and connectivity of sandstone and mudstone laminae at the appropriate length-
85 scale.

86 Two different methodologies have been used to create such models, which both use
87 stratigraphic surfaces to reproduce multi-scale heterogeneities. The first approach mimics
88 depositional processes by generating and translating bedforms with a particular geometry
89 according to user-defined inputs such as current velocity and sediment accumulation rate
90 through time (e.g. Rubin, 1987; Wen *et al.*, 1998; Rubin and Carter, 2005). Cross-
91 stratification is defined by the preserved remnants of the bedform-bounding surfaces, while
92 lithologies are distributed according to the local current velocities during deposition. This
93 process-based methodology has been used to generate highly realistic models of near-
94 wellbore regions (with dimensions of the order 0.3 x 0.3 x 2 m) (Nordahl *et al.*, 2005;
95 Ringrose *et al.*, 2005). However, process-based methodologies suffer from two problems.
96 First, the models cannot be conditioned directly to data available from outcrop or subsurface
97 measurements. Second, the required input parameters describing ancient depositional

98 properties, such as variations in current velocity and sediment availability, are highly
99 uncertain and have to be selected so as to produce a model that matches the preserved rock
100 architecture observed in core or outcrop; this is a complex and non-unique inversion
101 problem that is difficult to solve.

102 The second approach uses geometric and lithologic data from the subsurface in
103 conjunction with outcrop analogs to directly condition reservoir models (e.g. White and
104 Barton, 1999; Willis and White, 2000; White *et al.*, 2004; Jackson *et al.*, 2009; Sech *et al.*,
105 2009). Jackson *et al.* (2005) generated 3D models of rock samples (with dimensions of order
106 0.5 x 0.5 x 0.3 m) from heterolithic tidal sandstones observed at outcrop using serial 2D
107 sectioning, scanning and surface reconstruction techniques. Their methodology yields
108 models that are directly conditioned to observed geologic data, but its application relies on
109 selection of an appropriate analog (or analogs) for the reservoir facies to be characterized.
110 Furthermore, such a method is time-consuming, difficult to replicate, and leads to the
111 creation of deterministic models that do not capture uncertainty in sandbody proportions,
112 geometry and connectivity.

113 In this study, a surface-based modeling workflow is presented, which is then used to
114 produce stochastic models of heterolithic, cross-bedded tidal sandstones conditioned to
115 outcrop or subsurface data. A cross-bedding template surface is used in order to define and
116 populate a rock volume. The 3D morphology of the template surface is defined by purely
117 geometric input parameters that, in the case documented herein, were defined using
118 measurements from an outcrop analog (the Eocene Dir Abu Lifa Member, Western Desert,
119 Egypt; Bown and Kraus, 1988; Legler *et al.*, 2013). The models incorporate three of the four
120 hierarchical levels of heterogeneity for heterolithic tidal sandstone reservoirs described

121 above: (1) lamina boundaries and reactivation surfaces, (2) erosional bases of beds and
122 bedsets, and (3) boundaries between facies and facies associations. The paper has four
123 objectives. First, we present the new surface-based modeling workflow. Second, we identify
124 the geometric input parameters required for the modeling process and extract a range of
125 values for these parameters from statistical analysis of the outcrop analog dataset. Third, we
126 describe two generic models that reproduce: (1) trough cross-bedding dominated by muddy
127 toesets and with a relatively low sandstone content (89%), and (2) tabular cross-bedding
128 dominated by sandy foresets and with a higher sandstone content (94%). Finally, we use
129 flow-simulation to calculate the effective permeability of the models in order to
130 demonstrate the effectiveness of the surface-based modeling workflow and its application
131 to build models suitable for flow simulation. In a companion paper (Massart *et al.*, 2016, this
132 issue), the surface-based methodology has been used to create a set of mini-models in order
133 to investigate the range of effective permeability in heterolithic cross-bedded tidal
134 sandstone facies.

135

136 **Methodology**

137 ***Model-construction methodology***

138 The stratigraphic surfaces that define sedimentary structures within tidal sandstone
139 reservoirs can be categorized by their 3D geometries, irrespective of length scale: (1) planar
140 surfaces (parallel bedding; erosional or conformable facies contacts), (2) concave-upward
141 surfaces (sigmoidal bedding or cross bedding structures; channelized erosional contacts), or
142 (3) wavy surfaces (wavy-bedding, lenticular-bedding and flaser-bedding structures; irregular
143 erosional contacts). The surface-based methodology uses these scale-independent

144 stratigraphic surface geometries by modeling rock volumes within which surfaces share a
145 common geometric template. This methodology comprises the following three steps (Figure
146 1).

147 (1) The volume of rock to be modeled is subdivided into “elemental volumes” delimited
148 by a basal and a top surface. In each elemental volume, the heterogeneities are associated
149 with stratigraphic surfaces that have the same 3D geometry. The elemental volumes have
150 uniform shapes, but their dimensions can be varied. The model volume is filled with
151 elemental volumes until an appropriate 3D density is reached, in an approach analogous to
152 object-based modeling (e.g. Haldorsen and Damsleth, 1990). Rules of superposition and
153 erosion are applied to the elemental volumes to mimic their chronostratigraphic ordering.
154 For example, if the elemental volumes represent erosionally-based sediment bodies, then
155 each elemental volume is eroded by the basal surfaces of “younger” elemental volumes.

156 (2) Each elemental volume contains only one type of stratigraphic surface, the geometry
157 of which is defined by a “template surface”. The 3D geometry of the template surface is
158 defined mathematically. Each elemental volume is then filled with numerous stratigraphic
159 surfaces derived from the single template surface, following rules introduced by the user to
160 define, for example, the vertical and horizontal surface spacing. The vertical and lateral
161 extent of the surfaces within each elemental volume is controlled by the vertical and lateral
162 extent of the elemental volume.

163 (3) Once every elemental volume has been filled with template surfaces, a facies code is
164 assigned to the geologic domains defined by the surfaces, or to the surfaces themselves. The
165 facies codes constrain the modeling of fine-scale petrophysical properties such as porosity
166 and permeability.

167 (4) The surface-based model is then gridded for flow simulation. The grid is constructed
168 around the stratigraphic surfaces, in order to retain the geometries defined by the surfaces
169 and minimize the number of active grid cells required for flow simulation (Jackson *et al.*,
170 2005, 2009, 2013, 2015; Sech *et al.*, 2009). The resulting models are geometrically accurate
171 and computationally efficient, although the complex grid architectures may introduce
172 numerical artefacts in conventional reservoir simulators (described in more details in
173 Massart *et al.*, 2016; see also Graham *et al.*, 2015).

174

175 ***Application to heterolithic, cross-bedded tidal sandstones***

176 The three-step methodology described above is applied herein to the modeling of
177 heterolithic, cross-bedded tidal sandstones (Figure 1). Cross-bedded sandstones are
178 common in a wide range of depositional environments, including those influenced by tides
179 (e.g. Harms *et al.*, 1982; Rubin, 1987; Ashley, 1990). Cross-beds result from the migration of
180 dunes (or megaripples *sensu* Allen, 1968, or sand waves *sensu* Allen, 1980) in response to a
181 unidirectional current. Dunes develop straight crests (2D dunes) under low current
182 velocities, and sinuous or discontinuous crests (3D dunes) under higher current velocities
183 (Dalrymple *et al.*, 1978; Allen, 1980; Elliott and Gardiner, 1981; Middleton and Southard,
184 1984). Any dip-section (parallel to the main current direction) gives the same geometry for
185 tabular (or planar) cross-beds resulting from the migration of 2D dunes, whereas trough
186 cross-beds resulting from the migration of 3D dunes have a more variable dip-section
187 geometry. Each migrating dune is preserved as a cross-bed set with an erosional base, whose
188 geometry and extent reflect the morphology and trajectory of the scoured area in front of
189 the migrating dune. In the case of 2D dunes, the unidirectional current is dispersed along a

190 large area downstream of the dune crest, such that an extensive planar erosion surface of
191 low scour capacity is formed (Harms *et al.* 1982). In the case of 3D dunes, the current is
192 focused downstream of the migrating dune into scour pits, which migrate to produce a
193 curved, concave-upwards erosion surface (Dalrymple *et al.*, 1978; Harms *et al.*, 1982). Cross-
194 beds produced by dune migration are commonly stacked into larger sediment bodies of
195 characteristic internal architecture. For example, the deposits of larger bedforms, such as
196 bars, accumulate via the accretion of cross-beds that record the migration of smaller,
197 superposed bedforms, such as dunes and ripples, across the bar surface. Tidal bars migrate
198 laterally into adjacent channels due to changes in tidal flow patterns or interactions with
199 other processes (e.g. variations in wave climate or fluvial discharge). Consequently, tidal bar
200 deposits can be comprised entirely of stacked cross-bed sets, corresponding to the
201 preserved remnants of repeated dune migration (Allen, 1980; Dalrymple, 1984; Ashley,
202 1990).

203

204 ***Modeling of elemental volumes***

205 A volume of 9 m³ (3 x 3 x 1 m) of cross-bedded sandstone is considered in this study; in a
206 companion paper (Massart *et al.*, 2016), we demonstrate that this volume comfortably
207 exceeds the minimum volume (the representative elementary volume or REV) required to
208 calculate representative values of effective permeability in these dune scale cross-bedded
209 heterolithic units. At this length scale, the elemental volumes comprise tabular and trough
210 cross-bed sets, representing the preserved parts of 2D and 3D dunes in a tidal bar
211 succession, respectively. In each cross-bed set, the key heterogeneities captured are
212 mudstone drapes along foreset-toeset surfaces and each set corresponds to an elemental

213 volume. The model volume of 9 m³ here samples approximately 6 cross-bed sets and 600
214 foreset-toeset surfaces, based on outcrop-analog data presented in a later section.

215 Cross-bed set boundaries correspond to the preserved remnants of the erosional surface
216 developed downcurrent of migrating 2D- or 3D-dunes (Figure 2 A). Observations of modern
217 tidal dunes show that this erosional surface has a curved, elliptical shape in the strike
218 direction (orthogonal to the main paleocurrent direction, Figure 2 B). As the dunes migrate,
219 the resulting erosional surface is a downstream-amalgamated composite of the elliptical
220 strike-sections that record the successive positions of the deepest part of the scour pool in
221 front of the dune (Figure 2 B). In order to mimic the 3D geometry of this composite erosional
222 surface, the corresponding elemental volumes have been modeled here as ellipsoids (Figures
223 3, 4). The model volume is thus subdivided into ellipsoidal elemental volumes that
224 correspond to cross-bed sets, with tops that are truncated by the basal surfaces of overlying
225 elemental volumes (Figure 1 B). The elemental volumes are modeled stochastically using the
226 input parameters summarized in Table 1. For each parameter, the modeling algorithm can
227 use a single value, or a distribution characterized by a mean value and a standard deviation.

228

229 ***Modeling template surfaces within elemental volumes***

230 Each ellipsoidal elemental volume representing a cross-bed set contains multiple foreset-
231 toeset template surfaces of uniform geometry. The spacing of foresets and toesets, and their
232 associated mudstone drapes, is typically rhythmic, reflecting a hierarchy of periodic cycles in
233 tidal current velocity (e.g. Nio and Yang, 1991). The shortest tidal cycle is semi-diurnal (c. 12
234 hour period), and is characterized by the alternation of flood and ebb current stages,
235 separated by slack-water periods when the current velocity is zero. During slack-water

236 periods, mud particles and clay aggregates (flocs) are deposited to form mudstone drapes
237 over sandy bedforms (Allen, 1981; Dalrymple *et al.*, 2003). In an idealized semi-diurnal tidal
238 cycle, both the ebb and flood tides are recorded by deposition of a sand lamina on the lee
239 face (foreset) of a dune (Visser, 1980). Slack-water periods are recorded by mudstone drapes
240 that separate the foreset-toeset sandstone laminae representing the ebb-tidal and flood-
241 tidal currents. The tide is typically asymmetric, such that the ebb-tidal or flood-tidal currents
242 are either of unequal velocity or are physically separated around the bar form (Visser, 1980).
243 The dominant tide is represented by thicker foreset-toeset sandstone laminae and the
244 subordinate tide by either thinner laminae or erosion (reactivation) surfaces.

245 An idealized, fully preserved semi-diurnal tidal cycle is thus represented by two
246 sandstone laminae and two mudstone drapes (“paired mudstone drapes” or “mud couplet”;
247 Visser, 1980) that constitute one tidal bundle (Boersma, 1969). Longer tidal cycles, which are
248 commonly preserved as rhythmic variations in the thickness of sandstone laminae and
249 mudstone drapes within cross-bed sets, are diurnal (c. 24 hour period) and spring-neap
250 (c. 14 day period) cycles. Superposition of the different tidal cycles, combined with other
251 sediment transport processes, leads to preservation of sandy foresets and muddy toesets. A
252 vertical profile through dune toeset deposits typically exhibits rhythmic alternation of
253 millimeter- to centimeter-thick, wavy-bedded mudstone and sandstone laminae (Reineck
254 and Singh, 1967). The transition between the foreset and toeset of each lamina in a cross-
255 bed set is marked by a gradual reduced downcurrent curvature. The resulting foreset-toeset
256 geometry may be referred to as “shovel” shaped (Van den Berg *et al.*, 2007). In a dip-section,
257 the shape of the foreset part is therefore approximated by a parabolic curve, and that of the
258 toeset part is approximated by a straight line:

259

$$\begin{cases} \text{Foreset: if } x > 0, z(x) = Ax^2 \\ \text{Toeset: if } x < 0, z(x) = 0 \end{cases} \quad (1)$$

260 where x is the dip-direction coordinate, and z is the vertical coordinate, relative to the
 261 junction point O between the flat toeset part and the concave-upward foreset part (which is
 262 defined to be the origin, $x = 0, z = 0$). The whole toeset-foreset surface is then rotated by an
 263 angle α , which corresponds to the dip angle of the toeset. Equation (1) becomes:

264

$$\begin{cases} \text{Foreset: if } x > 0, z(x) = \frac{\cos \alpha - 2xA \cos \alpha \sin \alpha - \sqrt{\cos^2 \alpha - 4Ax \sin \alpha}}{2A \sin^2 \alpha} \\ \text{Toeset: if } x < 0, z(x) = x \tan \alpha \end{cases} \quad (2)$$

265 Notice that both equations have the same derivative $z'(x=0) = \tan \alpha$ at the junction point
 266 O , so that the curve is continuous from the toeset part to the foreset part of the surface.

267 In a strike section with coordinate y , the foreset and toeset geometry reflects the
 268 erosional scour at the base of the migrating dune, so that the resulting cross-section in the
 269 strike direction corresponds to trough or tabular cross-beds. Successive foreset-toeset
 270 surfaces are parallel to each other, and parallel to the erosional base of the cross-bed set
 271 (i.e. elemental volume). Consequently, equation (2) is generalized for any (x,y) direction:

272

$$\begin{cases} \text{Foreset: if } x > 0, z(x,y) = \left[\frac{\cos \alpha - 2xA \cos \alpha \sin \alpha - \sqrt{\cos^2 \alpha - 4Ax \sin \alpha}}{2A \sin^2 \alpha} \right] + \left[\sum_1^i T_{T_i} + B(x,y) \right] \\ \text{Toeset: if } x < 0, z(x,y) = [x \tan \alpha] + \left[\sum_1^i T_{T_i} + B(x,y) \right] \end{cases} \quad (3)$$

273 where $B(x,y)$ describes the 3D ellipsoidal shape of the basal surface of the cross-bed set (i.e.
 274 elemental volume):

275

$$B(x, y) = (H_E / 2) \sqrt{1 - \frac{x^2}{(L_E / 2)^2} - \frac{y^2}{(W_E / 2)^2}} \quad (4)$$

276

277 The term $\sum_1^i T_{Ti}$ corresponds to the cumulative toset thickness, with T_T corresponding to
 278 the individual toset thickness. Every cross-section of one foreset-toeset surface in the strike
 279 direction is an ellipse parallel to the erosional base of the cross-bed set. In particular, for
 280 $x = 0$, the strike cross-section curve links all junction points O of any given foreset-toeset
 281 surface, creating a junction line Oy , simplifying equations (3) and (4) to yield:

282

$$z(x = 0, y) = \sum_1^i T_{Ti} + (H_E / 2) \sqrt{1 - \frac{y^2}{(W_E / 2)^2}} \quad (5)$$

283

284 In order to populate the ellipsoidal elemental volumes with foreset-toeset template
 285 surfaces, the input parameters summarized in Table 1 are required (Figures 1 C, 5). Toeset
 286 thicknesses T_T (Figure 5) are generally too small to be routinely measured directly from cores
 287 and outcrop analogs with high accuracy (< 1 cm). Therefore we calculate T_T indirectly from
 288 two other parameters: the dip angle of the toesets α and the angle of dune climb δ (Figure
 289 5). The dip angle α corresponds to the angle of rotation applied to the parabolic curve
 representing the foreset-toeset template surface. T_T is then given by:

290

$$T_T = F_T \sin(\alpha + \delta) \quad (6)$$

291

292 ***Modeling of mudstone drapes along foreset-toeset surfaces***

293

294 If the succeeding flood-tide or ebb-tide is sufficiently strong, then mudstone drapes can
 be partially or entirely eroded, such that only one mudstone drape and one reactivation

295 surface may be preserved during one flood-and-ebb tidal cycle (de Mowbray and Visser,
 296 1984). Thus, the foreset-toeset surfaces modeled in the previous step may not be entirely
 297 covered by mudstone. The extent and continuity of mudstone drapes is defined using a
 298 function to describe the mudstone frequency in the dip direction along the stratigraphic
 299 surfaces, relative to a well-defined position on the surfaces. Mudstone drapes are modeled
 300 as elliptical patches of mudstone that are placed stochastically on each surface. Where they
 301 overlap, new patches erode older patches, so the patches coalesce to produce drapes with
 302 complex geometries. The length and aspect ratio of each elliptical patch is also modeled
 303 stochastically. Patches are placed on the stratigraphic surfaces until a user-specified
 304 proportion of their area is reached, following the methodology of Jackson and Muggeridge
 305 (2000). The mudstone frequency function denotes the probability that a patch will be placed
 306 at a certain location along each surface. The foreset part of each surface is modelled first;
 307 the mudstone drape coverage is then calculated at the transition between foreset and
 308 toeset parts (line Δ in Figure 5), and this calculated value is then used as the target
 309 mudstone drape coverage for the toeset parts, in order to ensure mudstone drape coverage
 310 continuity between the foreset and toeset parts. Consequently, toeset and foreset parts of
 311 each surface can have different mudstone drape coverage, allowing us to capture the muddy
 312 toesets typically observed in outcrop. The distribution of mudstone drapes along each
 313 surface is controlled by the chosen mudstone frequency function f , which is determined here
 314 from outcrop analog data. The following equation has been used to define f :

$$f\left(\frac{x-x_0}{x_f-x_0}\right) = \frac{M}{1+e^{\left(N\left(\frac{x-x_0}{x_f-x_0}\right)+0\right)}} \quad (7)$$

315

316 where x_o corresponds to the coordinate of the junction point O between foreset and toeset
317 sections, x_f corresponds to the coordinate of the point F marking the preserved top of the
318 foreset, and M , N and O are constants that are chosen to fit data extracted from the outcrop
319 analog. Such data could also be extracted from process-based models.

320 Mudstone drape thickness is user defined in the models and, at present, is assumed to be
321 constant for each drape. As mudstones are modeled as barriers to flow, their thickness has
322 no impact on their flow properties; however, drape thickness does affect the total volume of
323 the model that is occupied by mudstone. Here we have assumed a mud drape thickness of
324 3.5 mm, which is a typical mean value encountered in heterolithic cross-bedded tidal
325 sandstones (Terwindt, 1971; Nio and Yang, 1991; Martinius and Van den Berg, 2011).
326 Measurements of mudstone drape thickness could be taken from core datasets for
327 application to a specific reservoir, or from a suitable outcrop analog. The input parameters
328 required for modeling mudstone drapes are summarized in Table 1 (Figure 1 D).

329

330 ***Outcrop analog data analysis to define model input parameters***

331 The input parameters required to construct the models of heterolithic, cross-bedded
332 tidal sandstones were collected from an exceptionally well-exposed outcrop analog (see
333 below), which enabled the 3D geometry of the elemental volumes, template surfaces and
334 mudstone distribution to be evaluated quantitatively.

335 The studied outcrop analog forms part of the Eocene Dir Abu Lifa Member, located in the
336 Western Desert of Egypt (Figure 6). The Dir Abu Lifa Member was deposited in a shallow-
337 marine environment protected from wave energy, resulting in a predominance of tidal
338 processes (Abdel-Fattah *et al.*, 2010; Legler *et al.*, 2013). The lower part of the Dir Abu Lifa

339 Member consists largely of tidal bar and channel deposits that are stacked laterally and
340 vertically (Legler *et al.*, 2013). The lower parts of tidal bar deposits typically comprise
341 heterolithic, cross-bedded sandstones.

342 The lower Dir Abu Lifa Member is exposed in a continuous escarpment over 20 km long,
343 which is cut by multiple canyons that provide some three dimensional control (e.g. Legler
344 *et al.*, 2013). The datasets used in this study are taken from two locations, labelled Gecko
345 Nose and Butterfly Canyon in Figure 6. Gecko Nose is a small promontory which is defined by
346 two cliff faces that trend approximately WNW-ESE and SSW-NNE, nearly perpendicular to
347 each other (Figures 6, 7). The promontory exposes stacked trough and tabular cross-bedded
348 sandstones, interpreted as the deposits of tidal bars in a channel belt (the “yellow channel”
349 in the Gebel Sagha area of Legler *et al.*, 2013). The WNW-ESE-oriented cliff face (N110-N290)
350 is 17 m long, and the SSW-NNE-oriented cliff face (N030-N210) is 12 m long. Paleocurrent
351 measurements from the cross-beds are oriented towards N230, indicating that the WNW-
352 ESE- and SSW-NNE-oriented cliff faces provide close to strike and dip sections, respectively.
353 The slight deviation from the mean dip direction indicated by the paleocurrent data does not
354 significantly impact the geometry of the modeled cross-bed sets.

355 Butterfly Canyon contains a larger promontory than Gecko Nose, defined by two cliff
356 faces that trend approximately N-S and W-E. The Butterfly Canyon outcrop also exposes
357 stacked trough and tabular cross-bedded sandstones deposited in bars occupying an isolated
358 channel in a tidal flat environment (the Wadi Ghorab area of Legler *et al.*, 2013).
359 Paleocurrent measurements from the cross-beds are oriented towards N196, indicating that
360 the W-E- and N-S-oriented cliff faces again provide close to strike and dip sections,
361 respectively. Tidal bar deposits exposed at Butterfly Canyon are sandier than those at Gecko

362 Nose, and the two deposits are considered to be end-members of the same heterolithic,
363 cross-bedded tidal sandstone facies.

364 High-resolution photographs and precise sketches were collected from the cliff faces of
365 both localities, in order to capture the dimensions and geometries of cross-bed sets.
366 Photographs were collected using no-distortion lenses. Each cross-bed set in the Gecko Nose
367 outcrop has been reconstructed from the high-resolution photographs and scaled using the
368 sketches. The boundaries of the cross-bed sets and their constituent foreset-toeset surfaces
369 have been traced on the reconstructed pictures, enabling quantitative, statistically
370 representative datasets to be compiled for the various input parameters of the modeling
371 methodology described above. All values are summarized in Table 1.

372 To define the dimensions of ellipsoidal elemental volumes (L_E , W_E and H_E) we used data
373 from the Gecko Nose outcrop. W_E and H_E were determined from 12 trough cross-bed set
374 boundaries (identified in Figure 8 A) from the strike-oriented face, using the method
375 presented in Figure 4. The dataset was limited to cross-bed sets with sufficient exposure to
376 allow a best fit elliptical curve, with dimensions corresponding to W_E and H_E , to be fitted to
377 their erosional basal surfaces (Figure 4 C). L_E was estimated from cross-bed sets exposed on
378 the dip-oriented face. The basal boundaries of all trough cross-bed sets in the dip-oriented
379 face were continuous and nearly planar over the 12 m extent of the face, suggesting
380 $L_E \gg W_E$. No pinch-outs were observed. The elemental volume density D , was determined
381 from the total of 90 trough cross-bed sets observed at the Gecko Nose location within a
382 volume of 12 x 17 x 3 m, such that D is equal to 0.15 elemental volumes per m³. The
383 dimensions of the preserved parts of the ellipsoidal elemental volumes (L_A , W_A and H_A) were
384 determined using data from both outcrops. W_A and H_A were determined from the strike-

385 oriented face of Gecko Nose (Figure 8 B). Values of both W_A and H_A define log-normal
386 distributions (Figure 9). All of the cross-bed sets observed in the dip-oriented face of Gecko
387 Nose are laterally continuous, in which case $L_A > 12$ m. At Butterfly Canyon, L_A is observed in
388 one cross-bed set to equal 25 m, which is the value used thereafter.

389 In order to determine the degree of curvature A , the 90 foreset-toeset surfaces
390 contained in three well-preserved trough cross-bed sets in the Gecko Nose outcrop
391 (numbered 34, 50 and 52 in Figure 8 A) have been extracted from photomontages. The three
392 cross-bed sets show clear, dip-oriented cross-sections of the foreset-toeset surfaces. The
393 foreset-toeset surfaces are rotated in our analysis so that their toesets are horizontal. For
394 each foreset-toeset surface, the junction point O is identified. All the foreset curves are then
395 translated to the same origin and a best-fit parabolic curve is fitted to the data (Figure 10).
396 To determine the foreset thickness F_T , the sandstone laminae thicknesses comprised
397 between the 544 foreset-toeset surfaces contained in 12 studied cross-bed sets (identified in
398 Figure 8 A) have been measured after extraction of the surfaces from photomontages. A log-
399 normal distribution of F_T values is observed (Figure 11). The dip angle of the toesets α has
400 been measured on photopanoramas of the NNE-SSW-oriented (oblique dip-oriented) face of
401 Gecko Nose. The angle of dune climb δ has been determined by generating a best-fit line
402 through the foreset-to-toeset junction points O of laminae in each of the studied cross-bed
403 sets.

404 To define the mudstone frequency function f , the positions of mudstone drapes along
405 the same 90 foreset-toeset surfaces of the three cross-bed sets used to determine the
406 parameter A (numbered 34, 50 and 52 in Figure 8 A) have been extracted from
407 photomontages. From this dataset, a frequency distribution of mudstone drape presence

408 relative to position along the foreset has been determined using equation (7) to define a
409 best-fit curve (Figure 12).

410

411 **Results**

412 ***Models constructed from outcrop analog data***

413 The 3D models of heterolithic, cross-bedded tidal sandstones are based on those
414 observed at the Gecko Nose and the Butterfly Canyon localities. Generic models have been
415 generated using input parameters derived from both localities (Figures 13 and 14; Table 1).
416 The models are stochastically generated using the data reported in the previous section,
417 except for the elemental volumes, whose coordinates inside the model are extracted directly
418 from photomontages of the two outcrop localities so that the traces of the elemental
419 volumes in cross-sections of the model accurately reproduced the cross-bed set boundaries
420 of the outcrop sections. Both models are 9 m^3 in volume ($3 \times 3 \times 1 \text{ m}$), and contain four
421 partially preserved ellipsoidal elemental volumes in the case of the Butterfly Canyon model
422 and six partially preserved ellipsoidal elemental volumes in the case of the Gecko Nose
423 model. The model volumes are approximately five orders of magnitude larger than the
424 volume of a typical core plug (c. 20 cm^3). Around 500 foreset-toeset surfaces are populated
425 in in the Gecko Nose model, whereas only 170 of the same surfaces are present in the
426 Butterfly Canyon model (parameter N_{CB} in Table 1). Note that the two outcrop localities
427 both display examples of tabular and trough cross bedding. However, the Gecko Nose
428 model shown here contains only trough cross-beds, and the Butterfly Canyon model
429 contains only tabular cross-beds, reflecting the specific parts of the outcrops modelled. The
430 mudstone drape coverage that was chosen for both models is equal to 25% along the foreset

431 parts and 57% along the toset parts of the foreset-toset surfaces; the foreset drape
432 coverage was extracted from outcrop data, while the toset drape coverage is given by the
433 fraction at the foreset-toset junction resulting from the chosen mudstone frequency
434 function (Figure 12), as outlined in the methodology.

435 A comparison between the outcrop cliff faces of Gecko Nose and Butterfly Canyon, and
436 the corresponding generic models is presented in Figure 15. The models honor the geometry
437 of the cross-bed set boundaries, in both strike and dip directions, which validates the choice
438 of having cross-bed sets represented as ellipsoidal elemental volumes (Figures 2, 3 and 4).
439 The input average foreset thickness F_T is respected as observed at the outcrop locations,
440 with F_T being smaller for the Gecko Nose model than for the Butterfly Canyon model. The
441 Gecko Nose model is relatively mudstone-rich (sandstone volume fraction $V_S/V_T = 0.89$), as it
442 comprises trough cross-beds containing a relatively high proportion of tosets and thin
443 foresets (foreset thickness $F_T = 5.85$ cm and foreset to toset volume ratio $R_{F/T} = 6.5 : 1$,
444 Table 1) due to the high dune climb angle of $\delta = 5^\circ$. The Butterfly Canyon model is
445 comparatively mudstone-poor (sandstone volume fraction $V_S/V_T = 0.94$), as it comprises
446 tabular cross-beds dominated by thicker foresets (foreset thickness $F_T = 10.0$ cm and foreset
447 to toset volume ratio $R_{F/T} = 24 : 1$, Table 1), with a low dune climb angle $\delta = 0^\circ$.

448 The distribution of mudstone drapes along the cross-bedding surfaces closely matches
449 the distribution observed at outcrop. Both in the models and at outcrop, some mudstone
450 drapes appear continuous along the entire cross-bedding surface, from the toset part to
451 the top of the foreset at the top boundary of the cross-bed set. In most cases, the mudstone
452 drapes in the models are discontinuous over the entire length of the cross-bedding surfaces
453 in dip-oriented cross-sections, but the discontinuities are limited in the strike direction,

454 which is again a close match to outcrop observations. Discontinuities of the mudstone
455 drapes in the models are mostly located at the top of the foreset part of the cross-bedding
456 surfaces, following the trend of the input mudstone drape frequency function defined from
457 statistical analysis of outcrop data (Figure 12).

458

459 **Calculation of effective permeability**

460 The method to calculate effective permeability is presented in the companion paper
461 (Massart *et al.*, 2016) and we report only the results here for the two models shown in
462 Figures 13 and 14. We report the effective permeability as a normalized value, expressed as
463 a fraction of the sandstone permeability:

$$464 \quad k_e^n = \frac{k_e}{k_{sand}} \quad (8)$$

465 The results reported in this way are independent of the value of sandstone permeability
466 used in the models; moreover, the normalized effective permeability can be rescaled to any
467 value of sandstone permeability obtained from core or mini-permeameter measurements.

468 The effective permeability of the model volume has been extracted in three orthogonal
469 directions: the horizontal effective permeability down depositional dip k_d , the horizontal
470 effective permeability along depositional strike k_s , and the vertical effective permeability k_v .
471 The mean value for horizontal permeability k_h is defined as the arithmetic average between
472 k_s and k_d such as $k_h = (k_d + k_s)/2$ (Jackson *et al.*, 2003). The results for each model are
473 summarized in Table 2. Despite the relatively low fraction of mudstone in the models, the
474 presence of the mudstone drapes significantly reduces both horizontal and vertical
475 permeabilities, and introduces permeability anisotropy in the horizontal as well as the

476 vertical directions : $k_s \neq k_d$ and $k_v \ll k_h$. For the trough-cross bedded model of Gecko Nose,
477 the dip-oriented horizontal permeability ($k_d^n = 47.5\%$) is only 65% of the strike-oriented
478 horizontal permeability ($k_s^n = 72.8\%$), as the flow must cross a larger number of mudstone-
479 draped foresets when flowing down depositional dip as opposed to along depositional strike.
480 The k_v/k_h ratio is reduced to only 0.040, reflecting that vertical flow must also cross
481 numerous mudstone-draped foresets. The horizontal permeability anisotropy of the tabular
482 cross-bedded Butterfly Canyon model is less pronounced than in the trough-cross-bedded
483 Gecko Nose model, reflecting the lower mudstone fraction and greater strike-oriented
484 continuity of foreset-toeset sandstone laminae in the former model: the dip-oriented
485 horizontal permeability ($k_d^n = 70.0\%$) is 78% of the strike-oriented horizontal permeability
486 ($k_s^n = 90.0\%$). Despite the lower overall mudstone fraction, the k_v/k_h of the tabular cross-
487 bedded Butterfly Canyon model is one order of magnitude smaller (at 0.003) than the value
488 of the trough cross-bedded model. Mudstone drapes are approximately three times more
489 numerous in the trough cross-bedded model ($N_{CB} \approx 500$) than in the tabular cross-bedded
490 model ($N_{CB} \approx 170$); they are more densely spaced and laterally continuous in the toesets of
491 the trough cross-bedded model because of the high values of the toeset dip angle α .
492 Moreover, the sandstone volume fraction in the toesets of the tabular cross-bedded model
493 is 0.26, which is less than half of the sandstone volume fraction in the toesets of the trough
494 cross-bedded model, despite the common value of mudstone drape coverage of 57% in both
495 models. The smaller value of k_v/k_h ratio in the tabular cross-bedded model arises from the
496 closer spacing of mudstone-draped toesets, higher density of toeset surfaces, and
497 consequent lower sandstone volume fraction in the toeset parts of cross-bed sets.

498 For the two models studied, the normalized effective permeability values can be rescaled
499 to any measured sandstone permeability to yield estimates of effective permeability suitable

500 for use in larger-scale reservoir models (Figure 16). For example, if the measured
501 permeability of the sandstone was 500 md, then the trough-cross bedded (Gecko Nose)
502 model yields permeability values of $k_d = 238$ md, $k_s = 364$ md and $k_v = 12$ md, while the
503 tabular cross-bedded (Butterfly Canyon) model yields permeability values of $k_d = 350$ md,
504 $k_s = 450$ md and $k_v = 10$ md. If the permeability of the sandstone was lower at 100 md,
505 effective permeabilities are proportionately reduced as well, yielding $k_d = 48$ md, $k_s = 73$ md
506 and $k_v = 3$ md for the trough cross-bedded model, and $k_d = 70$ md, $k_s = 90$ md and $k_v = 2$ md
507 for the tabular cross-bedded model. Effective permeability values from a broader range of
508 model geometries and mudstone fractions are reported in the companion paper (Massart
509 *et al.*, 2016).

510 The modeling workflow reported here can be applied to create appropriate models for
511 the calculation of effective permeability values depending on the geometric characteristics
512 of the heterogeneity surfaces of any tidal cross-bedded heterolithic sandstone observed at
513 outcrop location or in subsurface. The required input parameters and methods for
514 measuring each of them are summarized in Figure 1. The main orientation of cross-bed sets
515 (i.e. the paleocurrent) and its standard deviation can be deduced from dipmeter logs. The
516 style of cross-bedding is easily recognizable from the trace of the cross-bedding plane
517 around the core or from borehole image logs. The tracing of the cross-bedding plane on well
518 imagery can be considered for more precision, as core observations are typically only
519 possible on one half of the core. The foreset thickness F_T can be measured on core from a
520 representative number of occurrences, even if the typical width of a core (8 – 20 cm)
521 prevents observation of a complete spring-neap cycle that displays cyclical variation of
522 foreset thickness. The foreset to toeset ratio $R_{F/T}$ can be appraised in a similar way from core
523 observations, but with similar limitations on the degree to which core data can represent

524 variation in the parameter. For both parameters, an outcrop analog(s) can provide a more
525 complete dataset. As dune climb angle δ has typically small values, the ratio $R_{F/T}$ remains
526 relatively uniform in the cross-bed set (Figures 3, 5). However, no lateral variation in $R_{F/T}$ can
527 be deduced from core observations. Finally, the toeset dip angle α can be observed in core if
528 toeset areas are sampled. All input parameters can be otherwise derived from statistical
529 analysis of appropriate outcrop analogs, in a similar way to the analysis presented herein
530 using the Dir Abu Lifa Member as an outcrop analog, with the important proviso that the
531 degree of analogy between subsurface and outcrop cases must be established with due care.

532

533 **Conclusions**

534 This study presents a novel reservoir modeling methodology that accurately and
535 efficiently reproduces the geometry and connectivity of sandstone and mudstone layers in
536 heterolithic, cross-bedded tidal sandstones by stochastically modeling stratigraphic surfaces
537 and associated heterogeneity. The model input parameters are geometric and can be
538 derived from subsurface cores and/or outcrop analog observations. The application of the
539 modeling methodology is demonstrated via the construction of models that represent
540 heterogeneity in significantly larger volumes (9 m^3) than those sampled by core plugs
541 (c. 20 cm^3), using input parameters derived from analysis of an outcrop analog. Quantitative
542 outcrop-analog data are collated and used to constrain the geometry and spatial distribution
543 of the small-scale heterogeneity surfaces (i.e. cross-bed set boundaries, cross-bedding
544 foreset-toeset surfaces, and mudstone drapes). The resulting models are a close visual
545 match to the outcrop data, such that the complex mudstone and sandstone connectivity of
546 the heterolithic tidal deposits is accurately reproduced. The surface-based methodology is

547 not dependent on length scale, but on the geometric configuration and hierarchical
548 arrangement of geologic surfaces. The methodology can, therefore, be applied to a much
549 wider range of reservoir types in which the heterogeneity style can be characterized by the
550 3D shape and distribution of geologic surfaces.

551

Preliminary
Version

552 **References cited**

- 553 Abdel-Fattah, Z. A., M. K. Gingras, M. W. Caldwell, S. G. Pemberton, 2010, Sedimentary
554 environments and depositional characteristics of the Middle to Upper Eocene whale-
555 bearing succession in the Fayum Depression, Egypt: *Sedimentology*, v. 7, n°2, p. 446-
556 476.
- 557
- 558 Allen, J. R. L., 1968, *Current ripples*, (Amsterdam) North-Holland.
- 559
- 560 Allen, J. R. L., 1980, Sand waves: a model of origin and internal structure: *Sedimentary*
561 *Geology*, v. 26, p. 281-328.
- 562
- 563 Allen, J. R. L., 1981, Palaeotidal speeds and ranges estimated from cross-bedding sets with
564 mud drapes: *Nature*, v. 293, p. 394-396.
- 565
- 566 Ashley, G. M., 1990, Classification of large-scale subaqueous bedforms; a new look at an old
567 problem *Journal of Sedimentary Petrology*, v. 60, p. 160-172.
- 568
- 569 Boersma, J. R., 1969, Internal structure of some tidal mega-ripples on a shoal in the
570 Westerschelde estuary, the Netherlands: *Geologie en Mijnbouw*, v. 48, p. 409-414.
- 571
- 572 Bown, T. M., and M. J. Kraus, 1988, Geology and paleoenvironment of the Oligocene Jebel
573 Qatrani Formation and adjacent rocks, Fayum depression, Egypt: U. S. Geological Survey
574 Professional paper 1452, p. 1–60.
- 575
- 576 Dalrymple, R. W., R. J. Knight, and J. J. Lambiase, 1978, Bedforms and their hydraulic stability
577 relationships in a tidal environment, Bay of Fundy, Canada: *Nature*, v. 275, p. 100-104.
- 578
- 579 Dalrymple, R. W., 1984, Morphology and internal structure of sand waves in the Bay of
580 Fundy: *Sedimentology*, v. 31, p. 365-382.
- 581
- 582 Dalrymple, R. W., E. K. Baker, P. T. Harris, and M. G. Hughes, 2003, Sedimentology and
583 stratigraphy of a tide-dominated, foreland-basin delta (Fly River, Papua New Guinea), *in*
584 *Tropical Deltas of Southeast Asia; Sedimentology, Stratigraphy, and Petroleum Geology*,
585 F. H. Sidi, D. Nummedal, P. Imbert, H. Darman, and H. W. Posamentier (eds), SEPM
586 Special Publication, v. 76, p. 147-173.
- 587
- 588 Dalrymple, R. W., and K. Choi, 2007, Morphologic and Facies Trends Through the Fluvial
589 Marine Transition in Tide Dominated Depositional Systems: a Schematic Framework for
590 Environmental and Sequence Stratigraphic Interpretation: *Earth Science Reviews*, v. 81,
591 issues 3-4, p. 135-174.
- 592
- 593 de Mowbray, T., and M. J. Visser, 1984, Reactivation surfaces in subtidal channel deposits,
594 Oosterschelde, Southwest Netherlands: *Journal of Sedimentary Petrology*, v. 54, p. 811-
595 824.
- 596

597 Elliott, T., and A. R. Gardiner, 1981, Ripple megaripple and sandwave bedforms in the
598 macrotidal Loughor Estuary, South Wales, U. K.: Special Publication International
599 Association of Sedimentologists, v. 5, p. 51-64.
600

601 Graham, G. H., Jackson, M. D., and Hampson, G. J., 2015: "Three dimensional modeling of
602 clinoforms within shallow-marine reservoirs: Part 1. Concepts and application: AAPG
603 Bulletin, v. 99, p. 1013-1047.
604

605 Haldorsen, H. H., and E. Damsleth, 1990, Stochastic modeling: Journal of Petroleum
606 Technology, v. 42, p. 404-412.
607

608 Harms, J. C., J. B. Southard and R. G. Walker, 1982, Structures and sequences in clastic rocks:
609 SEPM short course, v. 9, Society of Sedimentary Geology.
610

611 Jackson, M. D., and A. H. Muggeridge, 2000, The effect of discontinuous shales on reservoir
612 performance during immiscible flow: Society of Petroleum Engineers Journal, v. 5, p.
613 446-454.
614

615 Jackson, M. D., A. H. Muggeridge, S. Yoshida, and H. D. Johnson, 2003, Upscaling
616 permeability measurements within complex heterolithic tidal sandstones: Mathematical
617 Geology, v. 35, p. 499-520.
618

619 Jackson, M. D., S. Yoshida, A. H. Muggeridge, and H. D. Johnson, 2005, Three-Dimensional
620 Reservoir Characterisation and Flow Simulation of Heterolithic Tidal Sandstones: AAPG
621 Bulletin, v. 89, n°4, p. 507-528.
622

623 Jackson, M. D., G. J. Hampson and R. P. Sech, 2009. Three-dimensional modeling of a
624 shoreface-shelf parasequence reservoir analog: part 2. Geologic controls on fluid flow
625 and hydrocarbon recovery: AAPG Bulletin, v. 93, p. 1183-1208.
626

627 Jackson, M. D., J. L. M. A. Gomes, P. Mostaghimi, J. R. Percival, B. S. Tollit, D. Pavlidis, C. C.
628 Pain, A. H. El-Sheikh, A. H. Muggeridge, and M. J. Blunt, in press, Reservoir modeling for
629 flow simulation using surfaces, adaptive unstructured meshes and an overlapping
630 control-volume-finite-element method: Society of Petroleum Engineers Reservoir
631 Evaluation and Engineering.
632

633 Legler, B., H. D. Johnson, G. J. Hampson, B. Y. G. Massart, C. A.-L. Jackson, M. D. Jackson, A.
634 El-Barkooky, and R. Ravnås, 2013, Facies model of a fine-grained, tide-dominated delta:
635 Lower Dir Abu Lifa Member (Eocene), Western Desert, Egypt: Sedimentology, v. 60, p.
636 1313-1356.
637

638 Martinius, A. W., P. S. Ringrose, C. Brostrøm, C. Elfenbein, A. Næss, and J. E. Ringås, 2005,
639 Reservoir Challenges of Heterolithic Tidal Sandstone Reservoirs in Halten Terrace, mid-
640 Norway: Petroleum Geoscience, EAGE/Geological Society of London, v. 11, n°1, p. 3-16.
641

642 Martinius, A. W., and J. H. van den Berg, 2011, Atlas of sedimentary structures in estuarine
643 and tidally-influenced river deposits of the Rhine-Meuse-Scheldt system: EAGE
644 Publications BV, Houten, 298 p.
645

646 Massart, B. Y. G., M. D. Jackson, G. J. Hampson, and H. D. Johnson, 2016, Effective flow
647 properties of heterolithic, cross-bedded tidal sandstones: Part 2. Flow simulation, AAPG
648 Bulletin, this issue.
649

650 Middleton, G. V., and J. B. Southard, 1984, Mechanics of sediment movement: SEPM Short
651 course 3, Society of Sedimentary Geology (Tulsa), USA.
652

653 Nio, S.-D., and C.-S. Yang, 1991, Diagnostic Attributes of Clastic Tidal Deposits: a Review *in*
654 Clastic Tidal Sedimentology, Canadian Society of Petroleum Geologists, Memoir 16, p. 3-
655 28.
656

657 Nordahl, K., P. S. Ringrose, and R. Wen, 2005, Petrophysical Characterisation of a Heterolithic
658 Tidal Reservoir Interval Using a Process Based Modelling Tool: Petroleum Geoscience,
659 EAGE/Geological Society of London, v. 11, p. 17-28.
660

661 Nordahl, K., A. W. Martinius, and A. Kritski, 2006, Time-series analysis of a heterolithic,
662 ripple-laminated deposit (Early Jurassic, Tilje Formation) and implications for reservoir
663 modelling: Marine Geology, v. 235, n°1-4, p. 255-271.
664

665 Nordahl, K., and P. S. Ringrose, 2008, Identifying the Representative Elementary Volume for
666 Permeability in Heterolithic Deposits Using Numerical Rock Models: Math Geoscience, v.
667 40, p. 753-771.
668

669 Norris, R. J., and J. J. M. Lewis, 1991, The Geological Modeling of Effective Permeability in
670 Complex Heterolithic Facies: Society of Petroleum Engineers paper 22692, presented at
671 the 66th annual technical conference and exhibition, Dallas, TX, USA, 6-9 October 1991.
672

673 Reineck, H. E., and I. B. Singh, 1967, Primary sedimentary structures in the recent sediments
674 of the Jade, North Sea: Marine Geology, v. 5, p. 227-235.
675

676 Reineck, H. E., and F. Wunderlich, 1968, Classification and origin of flaser and lenticular
677 bedding: Sedimentology, v.11, n°1-2, p. 99-104.
678

679 Reineck, H. E., and I. B. Singh, 1980, Depositional sedimentary environments with reference
680 to terrigenous clastics, 2nd edition, Springer-Verlag (Berlin).
681

682 Ringrose, P. S., K. Nordahl, and R. Wen, 2005, Vertical Permeability Estimation of Heterolithic
683 Tidal Deltaic Sandstones: Petroleum Geoscience, EAGE/Geological Society of London, v.
684 11, n°1, p. 29-36.
685

686 Rubin, D. M., 1987, Cross-bedding, bedforms, and palaeocurrents: Concepts in
687 Sedimentology and Paleontology, Society of Economic Palaeontologists and
688 Mineralogists Special Publication, v. 1.

- 689
690 Rubin, D. M., C. L. Carter, 2005, Bedforms 4.0; MATLAB code for simulating bedforms and
691 cross-bedding: Open-File report, U. S. Geological Survey.
692
693 Sech, R. P., M. D. Jackson, and G. J. Hampson, 2009, Three-Dimensional Modelling of a
694 Shoreface-Shelf Parasequence Reservoir Analogue: Part 1. Surface-based Modelling to
695 Capture High Resolution Facies Architecture: AAPG Bulletin, v. 93, n°9, p. 1155-1181.
696
697 Terwindt, J. H. J., 1971, Lithofacies of inshore estuarine and tidal inlet deposits: Geologie en
698 Mijnbouw, v. 50, p. 515-526.
699
700 van den Berg, J. H., J. R. Boersma, and A. van Gelder, 2007, Diagnostic sedimentary
701 structures of the fluvial-tidal transition zone; Evidence from deposits of the Rhine and
702 Meuse: Geology en Minjbouw, v. 86, p. 287-306.
703
704 Visser, M. J., 1980, Neap-spring cycles reflected in Holocene subtidal large-scale bedform
705 deposits: a preliminary note: Geology, v. 8, p. 543-546.
706
707 Weber, K. J., 1986, How heterogeneity affects oil recovery *in* L. W. Lake, and H. B. Carroll Jr.
708 (eds), Reservoir characterization, Academic Press, New York, p. 487-544.
709
710 Wen, R.-J., A. W. Martinius, A. Næss, and P. S. Ringrose, 1998, Three dimensional simulation
711 of small-scale heterogeneity in tidal deposits – A process-based stochastic method *in* A.
712 Buccianti, G. Nardi, and A. Potenza (eds), Proceedings of the 4th Annual Conference of
713 the International Association of Mathematical Geology, Ischia, De Frede, Naples, p. 129–
714 134.
715 White, C. D., and M. D. Barton, 1999, Translating outcrop data to flow models, with
716 applications to the Ferron Sandstone: Society of Petroleum Engineers Reservoir
717 Evaluation and Engineering, v. 2, p. 341–350.
718
719 White, C. D., B. J. Willis, S. P. Dutton, J. P. Bhattacharya, and K. Narayanan, 2004,
720 Sedimentology, statistics, and flow behavior for a tide-influenced deltaic sandstone,
721 Frontier Formation, Wyoming, United States, in G. M. Grammer, P. M. Harris, and G. P.
722 Eberli, eds., Integration of outcrop and modern analogs in reservoir modeling: AAPG
723 Memoir 80, p. 129–152.
724
725
726
727
728

726 AUTHOR VITAE

- 727 Benoît Y. G. Massart works in the mature-area developments and increased oil recovery
728 team at the Statoil research center in Bergen, Norway. He holds a Ph.D. in petroleum

729 engineering from Imperial College London and a M.Sc. in petroleum geology from the École
730 Nationale de Géologie de Nancy (ENSG), France. His research interests are in reservoir
731 modeling and quantifying the influence of geologic heterogeneity on effective rock
732 properties and fluid flow behavior, facies modeling from geophysical data, and facies and
733 petrophysical property update in history matching in ensemble methods.

734

735 Matthew D. Jackson is the Total Professor of Geological Fluid Mechanics in the Department
736 of Earth Science and Engineering, Imperial College, London. He holds a B.S. degree in physics
737 from Imperial College and a Ph.D. in geological fluid mechanics from the University of
738 Liverpool. His research interests include simulation of multiphase flow through porous
739 media, representation of geologic heterogeneity in simulation models, and downhole
740 monitoring and control in instrumented wells.

741

742 Gary J. Hampson is a Reader in sedimentary geology in the Department of Earth Science and
743 Engineering, Imperial College, London. He holds a B.A. degree in natural sciences from the
744 University of Cambridge and a Ph.D. in sedimentology and sequence stratigraphy from the
745 University of Liverpool. His research interests lie in the understanding of depositional
746 systems and their preserved stratigraphy, and in applying this knowledge to reservoir
747 characterization.

748

749 Howard D. Johnson holds the Shell Chair of Petroleum Geology in the Department of Earth
750 Science and Engineering, Imperial College, London. His main interests are in clastic

751 sedimentology, sequence stratigraphy, reservoir characterization, and basin studies.
752 Previously, he spent 15 years with Shell working in research, exploration and development
753 geology, and petroleum engineering. He holds a B.Sc. degree in geology from the University
754 of Liverpool and a D.Phil. in sedimentology from the University of Oxford.

755

756 Berit Legler is a clastic sedimentologist with Wintershall, Germany. She graduated in geology
757 with a diplom degree and Ph.D. from the Technical University Mining Academy Freiberg,
758 Germany. She worked as sedimentologist with RWE Dea (2005 – 2008), post-doctoral
759 researcher at Imperial College London (2009 – 2011) and lecturer at the University of
760 Manchester (2011 – 2013). She currently works as sedimentologist in Wintershall's Reservoir
761 Geology technical services team.

762

763 Christopher A.-L. Jackson is currently the Statoil Professor of Basin Analysis in the
764 Department of Earth Science and Engineering, Imperial College, UK. He obtained a B.Sc. and
765 Ph.D. from the University of Manchester. His research interests are in the
766 tectonostratigraphic evolution of rifts and the application of 3D seismic data to
767 understanding the formation and filling of sedimentary basins.

768

769 **Figure captions**

770

771 **Figure 1:** Three-step methodology for constructing models of heterolithic, cross-bedded tidal
772 sandstones. A) Subdivision of the model volume into elemental volumes, in which
773 heterogeneities have the same length scale and geometry. In the cross-bedded sandstones
774 modeled here, the elemental volumes are cross-bed sets represented by ellipsoids with
775 erosional bases. Ellipsoid boundaries are represented by bold black lines. B) Each ellipsoid
776 (i.e. cross-bed set) is populated with template surfaces that represent foreset-toeset lamina
777 boundaries. Foreset-toeset template surfaces are represented by thin black lines. C) Each
778 foreset-toeset template surface is then lined by mudstone drapes of variable continuity,
779 using a mudstone frequency function, to produce D) the final model. Mudstone drapes are
780 represented by bold gray lines. For each step, the required input parameters are listed on
781 the right of the figure. Some parameters can be extracted from subsurface core data (*) or
782 dipmeter logs (†), whereas others must be taken from sedimentologic analogs.

783

784 **Figure 2:** A) Modern 3D dune in an inter-tidal flat environment, the Wash Estuary, United
785 Kingdom. B) Interpretation of the erosion surface resulting from migration of a dune and
786 associated scour pool as the lower part of an ellipsoid of dimensions L_E (length, in blue), W_E
787 (width, in red), and H_E (height, in green) relative to the horizontal reference plane Γ . Dotted
788 lines correspond to parts of the ellipsoid beneath the dune in its present position. The yellow
789 crescent corresponds to the dune foreset, and the gray truncated ellipse to the rippled dune
790 toeset. The bold black line corresponds to the dip cross-section of one foreset-toeset
791 surface.

792

793 **Figure 3:** A) Ancient trough cross-bed set viewed in cross-section oriented approximately
794 along depositional dip (parallel to the paleocurrent direction), Dir Abu Lifa Member, Gecko
795 Nose location (NNE-SSW-oriented cliff face shown with dotted line in Figures 6, 7), Western
796 Desert, Egypt. The cross-bed set contains tidal bundles separated by double mudstone
797 drapes in the sandy foresets, and wavy-bedded muddy toesets. B) Interpretation of the
798 cross-bed set as the lower part of an ellipsoidal elemental volume. The purple line shows the
799 erosional base of the cross-bed set, and the green line shows the top surface of the
800 preserved cross-bed set (i.e. the erosional base of an overlying cross-bed set). The thin
801 dotted line is the boundary between foresets and toesets within the cross-bed set marking
802 the angle of climb of the dune δ . The bold black line corresponds to an interpreted foreset-
803 toeset template surface in dip cross-section. C) The corresponding best fit ellipsoidal
804 elemental volume is traced in 3D (see Figure 2 for colors).

805
806 **Figure 4:** A) Ancient trough cross-bed set viewed in cross-section oriented approximately
807 along depositional strike (perpendicular to the paleocurrent direction which corresponds to
808 dip direction, here out of the page), Dir Abu Lifa Member, Gecko Nose location (WNW-ESE-
809 oriented cliff face shown with bold line in Figures 6, 7; see also Figure 8 A), Western Desert,
810 Egypt. B) Interpretation of the cross-bed set as the lower part of an ellipsoidal elemental
811 volume. The purple line shows the erosional base of the cross-bed set, and the green line
812 shows the top surface of the preserved cross-bed set. The dotted arrows indicate the
813 preserved width W_A and height H_A of the cross-bed set. The bold black line corresponds to an
814 interpreted foreset-toeset template surface in strike cross-section. C) The erosional base of
815 the cross-bed set has been extracted from the photomontage and a best fit elliptical curve

816 (in red) has been defined in order to obtain the width W_E and the height H_E of the elemental
817 volume.

818

819 **Figure 5:** Detail of transition between foreset and toset along template surfaces within an
820 elemental volume. Input parameters required to describe the geometry of the foreset-toeset
821 surfaces include foreset thickness F_T , toset thickness T_T , the angle of climb of the dune δ ,
822 and the dip angle of the toset α . The dotted line Δ corresponds to the limit between sandy
823 foresets (light gray) and muddy toesets (dark gray), and links the junction points O of each
824 foreset-toeset surface. The reference line Γ corresponds to the median plane of the
825 ellipsoidal elemental volume that contains the foreset-toeset surfaces (blue ellipse in Figure
826 2). Once F_T is set, T_T is calculated using angles α and δ (Equation (6)).

827

828 **Figure 6:** A. Map of Egypt highlighting the position of the Eocene Dir Abu Lifa outcrop belt
829 (black rectangle, south west of Cairo) B. Map of the main outcrop belt of the Dir Abu Lifa
830 Member, highlighting the Gecko Nose and Butterfly Canyon localities. C. Close-up of the
831 Gecko Nose outcrop, with the two studied cliff faces shown with bold lines, the continuous
832 line corresponding to the WNW-ESE oriented section, and the dotted line to the NNE-SSW
833 oriented cross-section (Figure 7).

834

835 **Figure 7:** Photograph of the two nearly perpendicular cliff faces at Gecko Nose (Figure 6).
836 Paleocurrents in heterolithic, trough and tabular cross-bedded sandstones are oriented
837 towards N196 (inset rose diagram), such that the WNW-ESE-oriented (bold line) and NNE-
838 SSW-oriented cliff faces (dotted line) approximate strike and dip sections, respectively. A
839 person is present in front of the outcrop for scale.

840

841 **Figure 8:** A) Photomontage of the WNW-ESE-oriented face of Gecko Nose (bold line face in
842 Figure 7), oblique to depositional strike. The 12 numbered trough cross-bed sets were
843 chosen to define best fit elliptical curves (cf. Figure 4). B) Interpretation of the
844 photomontage. Trough (gray) and tabular (yellow) cross-beds are numbered sequentially
845 and interpreted to be stacked vertically within a tidal bar deposit. Note that the numbering
846 starts at 10, as nine underlying cross-bed sets are exposed on the adjacent SSW-NNE-
847 oriented face (dotted line face in Figure 7).

848

849 **Figure 9:** Distribution of A) the preserved height H_A and B) preserved apparent width W_A of
850 49 trough cross-bed sets exposed on the WNW-ESE-oriented face of Gecko Nose (bold line
851 face in Figure 7; Figure 8 B), oblique to depositional strike. A log-normal distribution of the
852 form $\text{LogN}(\mu, \sigma^2)$ is interpreted, with parameters μ : mean value; σ : standard deviation. p
853 corresponds to the Kolmogorov-Smirnov test criterion: a value of 1 corresponds to a perfect
854 fit of the data with a log-normal distribution. For the height H_A in A), $\mu = 0.3$ cm and $\sigma =$
855 0.4 cm with $p = 0.82$; for the width W_A in B), $\mu = 3.1$ cm and $\sigma = 1.4$ cm with $p = 0.98$.

856

857 **Figure 10:** Point clouds defining the 90 foreset-toeset surfaces traced from three cross-bed
858 sets of the WNW-ESE-oriented face of Gecko Nose (numbered 34, 50 and 52 in Figure 8 A).
859 The surfaces are translated so that their foreset-to-toeset junction points (labelled O in
860 Figure 5) are superimposed, and a best-fit line for a foreset-toeset template surface is
861 determined (bold line). This line is described by equation (5) with the curvature parameter A
862 $= 5.5 \times 10^{-3}$, and the resulting line has a very strong correlation to the data ($R^2 = 0.98$).

863

864 **Figure 11:** Distribution of foreset thickness F_T for the 544 foreset-toeset surfaces of 12
865 studied cross-bed sets (Figure 8 A). A log-normal distribution of the form $\text{LogN}(\mu, \sigma^2)$ is
866 interpreted with parameters μ , mean value = 5.9 cm; σ , standard deviation = 2.0 cm.

867

868 **Figure 12:** Point cloud defining the coverage of mudstone drapes along 90 foreset-toeset
869 surfaces traced from three cross-bed sets (numbered 34, 50 and 52 in Figure 8 A). A best-fit
870 line for mudstone drape coverage along a foreset-toeset surface is determined (bold line).
871 This line is described by equation (4) with parameters $M = -1.004$, $N = -4.316$, and $O = 1.610$,
872 and it correlates very strongly to the data ($R^2 = 0.99$).

873

874 **Figure 13:** A) 3D view of the generic trough cross-bedding model, generated with input
875 parameters extracted from the Gecko Nose outcrop and summarized in Table 1. Only
876 mudstone drapes are displayed here and sandstone is removed from the model. The model
877 displays a mudstone drape coverage of 25% along the foreset parts, and a coverage of 57 %
878 along the toeset parts of the foreset-toeset surfaces. The trough aspect of the cross-bedding
879 appears in the strike direction. Warm colors indicate increasing height of mudstone drapes
880 above the cross-bed base, for each cross-bed set. B) Orthogonal sections through the same
881 model with mudstone and sandstone layers colored in black and yellow respectively. The
882 layers of mudstone have a constant thickness of 3.5 mm in the whole model. C) Dip-oriented
883 cross-section of the model presented in part A representing the cross-bedding surfaces. D)
884 The same dip-oriented cross-section but with the 25% mudstone drape coverage of foresets
885 and 57% mudstone drape coverage of toesets.

886

887 **Figure 14:** A) 3D view of the generic tabular cross-bedding model, generated with input
888 parameters extracted from the Butterfly canyon outcrop and summarized in Table 1. Only
889 mudstone drapes are displayed here and sandstone is removed from the model. The model
890 displays a mudstone drape coverage of 25% along the foreset parts, and a coverage of 57 %
891 along the toset parts of the foreset-toeset surfaces. B) Orthogonal sections through the
892 model. The layers of mudstone have a constant thickness of 3.5 mm in the whole model.
893 C) Dip-oriented cross-section of the model presented in part A representing the cross-
894 bedding surfaces. D) The same dip-oriented cross-section but with the 25% mudstone drape
895 coverage of foresets and 57% mudstone drape coverage of toesets. Same color schemes
896 than in Figure 13.

897

898 **Figure 15:** Comparison between outcrop photographs (top row), and corresponding cross-
899 sections of the surface-based models showing foreset-toeset surfaces (central row) and
900 mudstone drapes along these surfaces (bottom row). Column A) shows dip-oriented sections
901 from the Butterfly Canyon outcrop and model. Column B) shows strike-oriented sections
902 from the Gecko Nose outcrop and model (red rectangle in Figure 8 A).

903

904 **Figure 16:** Determination of effective permeability from the flow simulation results of the
905 two outcrop models (Figures 13, 14). If the studied heterolithic sandstone features trough
906 cross-bedding with muddy toset regions, the Gecko Nose model should be used for
907 reference; if the studied heterolithic sandstone features tabular cross-bedding with a
908 predominance of sandy foreset regions, the Butterfly Canyon model should be used. The two
909 examples of effective permeability derivation presented in the text are featured with

910 straight vertical lines: $k_{sand} = 500$ md and $k_{sand} = 100$ md. The resulting effective permeability
911 k_e can be read at the intersection of these straight lines with the different curves.

912

913 **Table captions**

914

915 **Table 1:** Input parameters for the Gecko Nose and Butterfly Canyon models (Figures 13, 14).

916

917 **Table 2:** Results for the Gecko Nose and Butterfly Canyon models (Figures 13, 14) after single
918 phase flow simulation. All measurements are dimensionless.

Preliminary
Version

Table 1:

Input parameter	Symbol	Unit	Trough cross-bedded model (Gecko Nose)	Tabular cross-bedded model (Butterfly Canyon)	Definition
Volume of the model	V_T	m^3	9	9	
Elemental volume length	L_E	m	20	20	Trough cross-beds are modelled as highly elongate, oblate ellipsoids with $L_E \gg W_E > H_E$. Tabular cross-beds are modelled as oblate ellipsoids with $W_E \geq L_E > H_E$, which yields laterally continuous sheets at the model scale (geometrical mean value $E[W_E] \pm$ standard deviation $\sigma[W_E]$).
Elemental volume width	W_E	m	4.85 ± 1.67	20	
Elemental volume height	H_E	m	1.35 ± 0.55	1.35 ± 0.55	
Preserved length of elemental volume	L_A	m	80% of L_E	100% of L_E	These parameters define the preserved aspect of the ellipsoidal elemental volumes in the model, after erosion at the base of overlying elemental volumes (geometrical mean value $E[W_A] \pm$ standard deviation $\sigma[W_A]$).
Preserved width of elemental volume	W_A	m	50% of W_E	100% of W_E	
Preserved height of elemental volume	H_A	m	30% of H_E	40% of H_E	
Elemental volume density	D	m^{-3}	6 elemental volumes in $9 m^3$	4 elemental volumes in $9 m^3$	Number of ellipsoidal elemental volumes present per unit volume of the model.
Elemental volume orientation	ϑ	$^\circ$	0	0	The azimuthal orientation angle ϑ of the ellipsoidal elemental volumes corresponds to the paleocurrent direction indicated by the foreset-toeset surfaces within a cross-bed set.
Number of cross-bedding surfaces	N_{CB}	-	≈ 500	≈ 170	
Parabolic curvature of foreset-toeset template surfaces	A	-	5.5×10^{-3}	5.5×10^{-3}	Characteristic coefficient of the square term for a parabolic curve, $z(x) = Ax^2$ as equation (1)

Foreset thickness	F_T	cm	5.85 ± 3.88	10 ± 3.88	Distance between two consecutive foreset-toeset surfaces, measured between their junction points O and O' (Figure 5).
Toeset dip angle	α	$^\circ$	8	1	Angle between the straight toeset surface and the median reference plane of the ellipsoidal elementary volume Γ (Figure 5)
Angle of dune climb	δ	$^\circ$	5	0	Angle between the median reference plane Γ and the boundary surface Δ which separates the foreset and the toeset parts in an elementary volume (Figure 5)
Foreset to toeset volume ratio	$R_{F/T}$	-	6.5 : 1	24 : 1	Ratio of the volume occupied by foreset by the volume occupied by toeset in the model
Mudstone frequency function	$f(M,N,O)$	-	Function f of Figure 12	Function f of Figure 12	Defined in 2D, along the azimuth of the ellipsoidal elemental volume (i.e. dip direction), according to the distance from the top of the foreset to the junction point O with the toeset. $M = -1.004$, $N = -4.316$, and $O = 1.610$ in equation (7)
Mudstone drape coverage	M_C	-	Foreset 25% Toeset 57%	Foreset 25% Toeset 57%	Mudstone patches are added along the foreset-toeset template surfaces until a specific proportion M_C of their area is covered.
Total area of the preserved foreset-toeset surface	A_F	cm ²	-	-	$M_C = A_M / A_F$
Area of the foreset-toeset surface covered by mudstone	A_M	cm ²	-	-	
Mudstone patch length	MP_L	cm	[0 – 20] Uniform distribution	[0 – 100] Uniform distribution	After the dimension of the major axis of the elliptical patch MP_L is defined, the dimension of the minor axis MP_W is randomly set as a fraction of MP_L
Mudstone patch width	MP_W	cm	[0 – 20] Uniform distribution Smaller than MP_L	[0 – 20] Uniform distribution Smaller than MP_L	

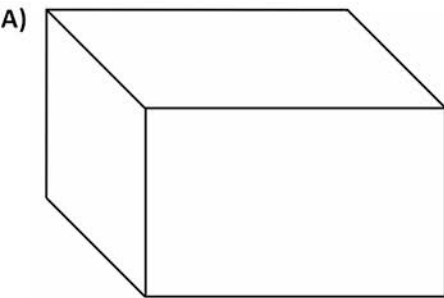
920 **Table 2:**

Measured parameter	Symbol	Trough cross-bedded model (Gecko Nose)	Tabular cross-bedded model (Butterfly Canyon)
Mudstone volume fraction	V_M/V_T	0.11	0.06
Sandstone volume fraction	V_S/V_T	0.89	0.94
Normalized effective dip horizontal permeability	k_d	47.5%	70.0%
Normalized effective strike horizontal permeability	k_s	72.8%	90.0%
Normalized effective vertical permeability	k_v	2.4%	2%
Ratio of vertical permeability by horizontal permeability	k_v/k_h	0.0399	0.0025

921

Preliminary
Version

Input parameters



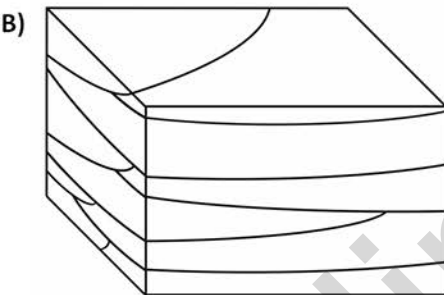
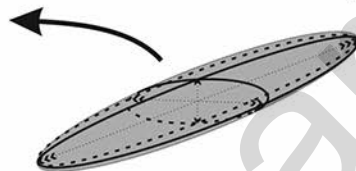
Ellipsoidal elemental volume

Dimensions: L_E, W_E, H_E

Cross-set density: D

Preserved dimensions: L_A, W_A, H_A^*

Cross-set orientation: θ^+
(Figures 2, 3, 4 and 9)



Foreset-toeset template surface

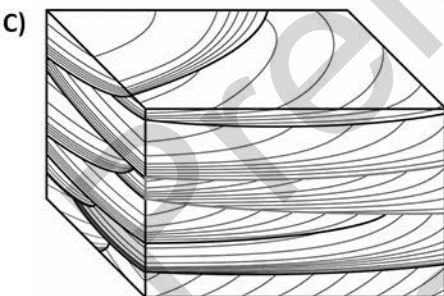
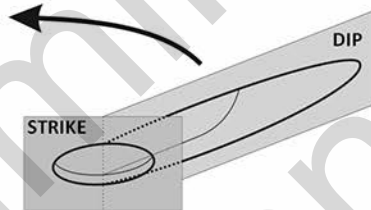
Parabolic curvature: A

Foreset thickness: F_T^*

Dip angle of the toeset: α^*

Dune climb angle: δ

(Figures 2, 3, 5, 10 and 11)



Mudstone drapes

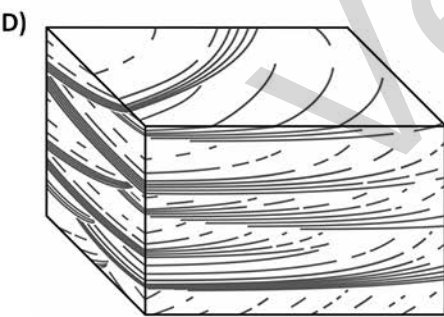
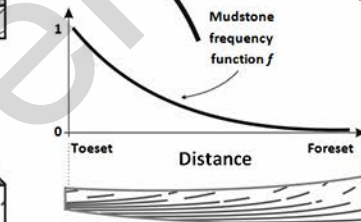
Mudstone frequency function: $f(M, N, O)$

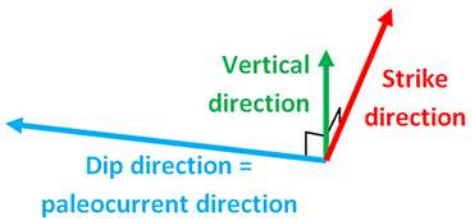
Mudstone drape coverage: M_C

Mudstone patch

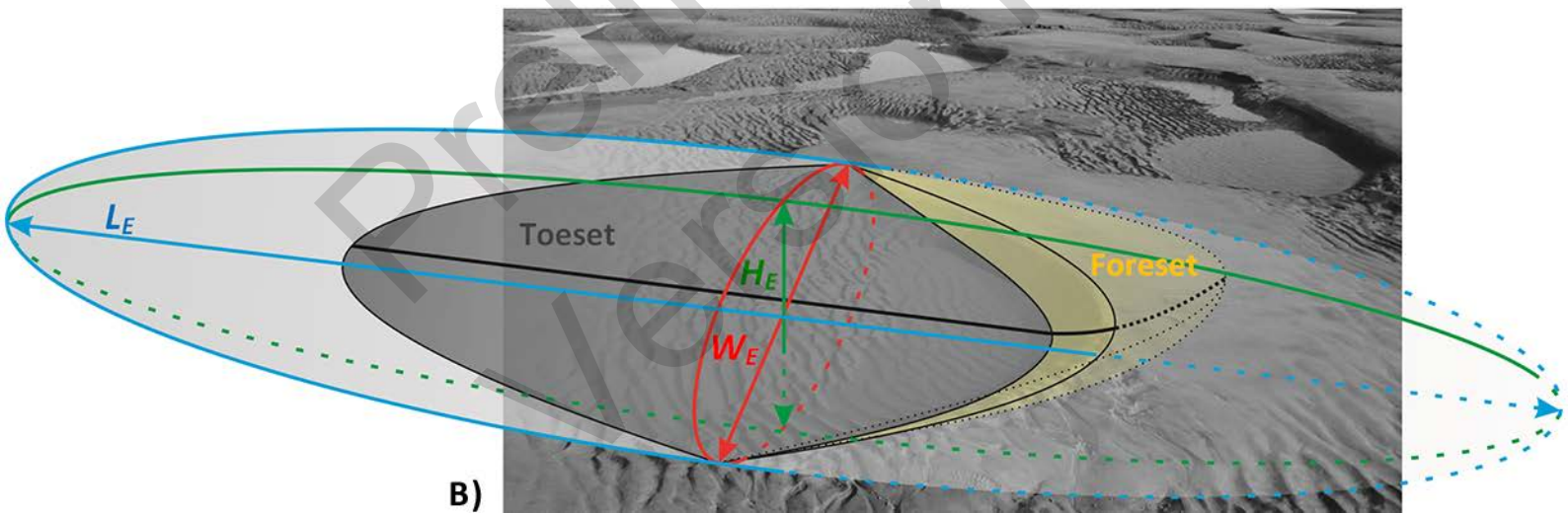
dimensions: MP_L, MP_W

(Figure 12)





A)

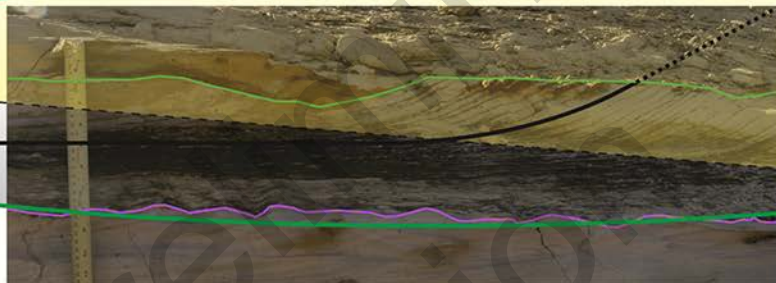


B)

A)



B)

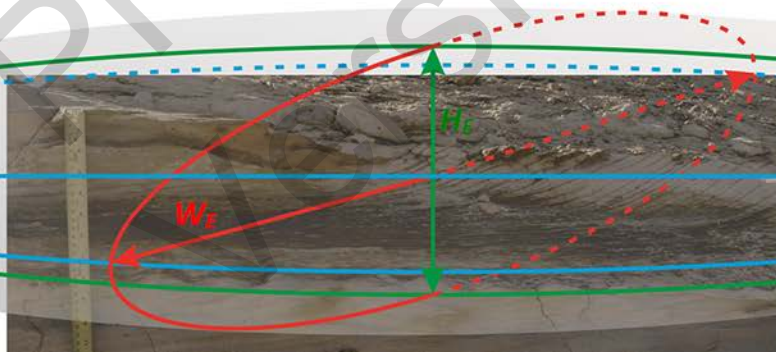


Top boundary
of the cross-bed set

Erosive base
of the cross-bed set

$\frac{\gamma}{\delta}$

C)



Foreset

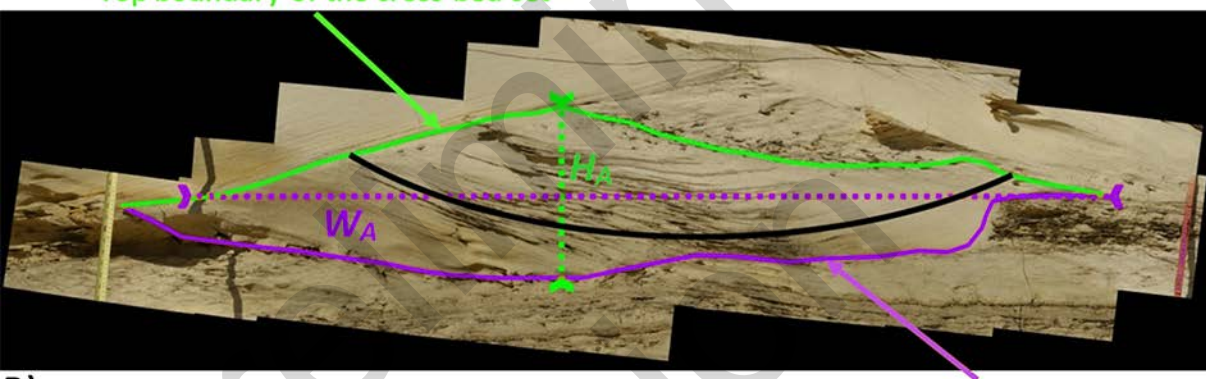
Toeset

 L_E W_F H_F

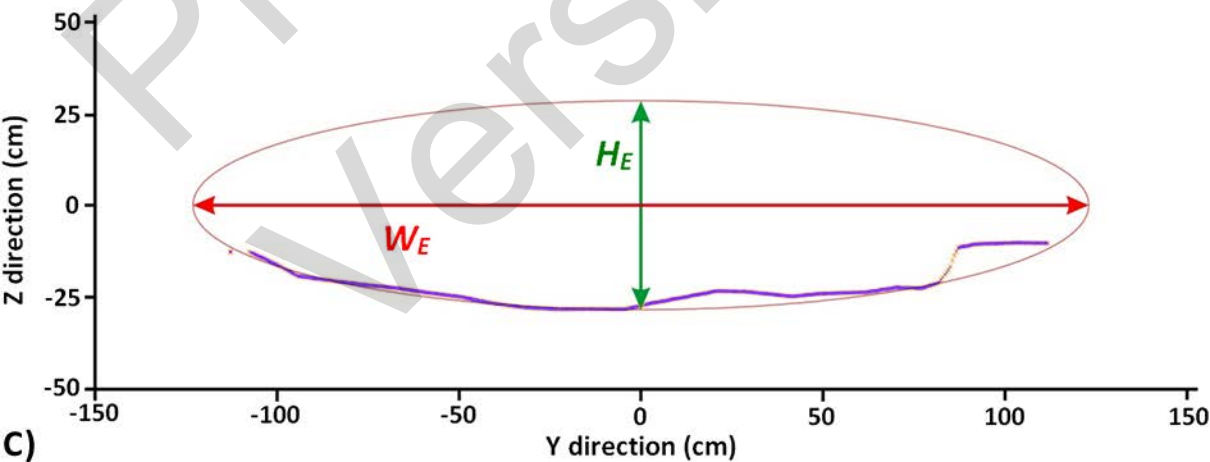


A)

Top boundary of the cross-bed set

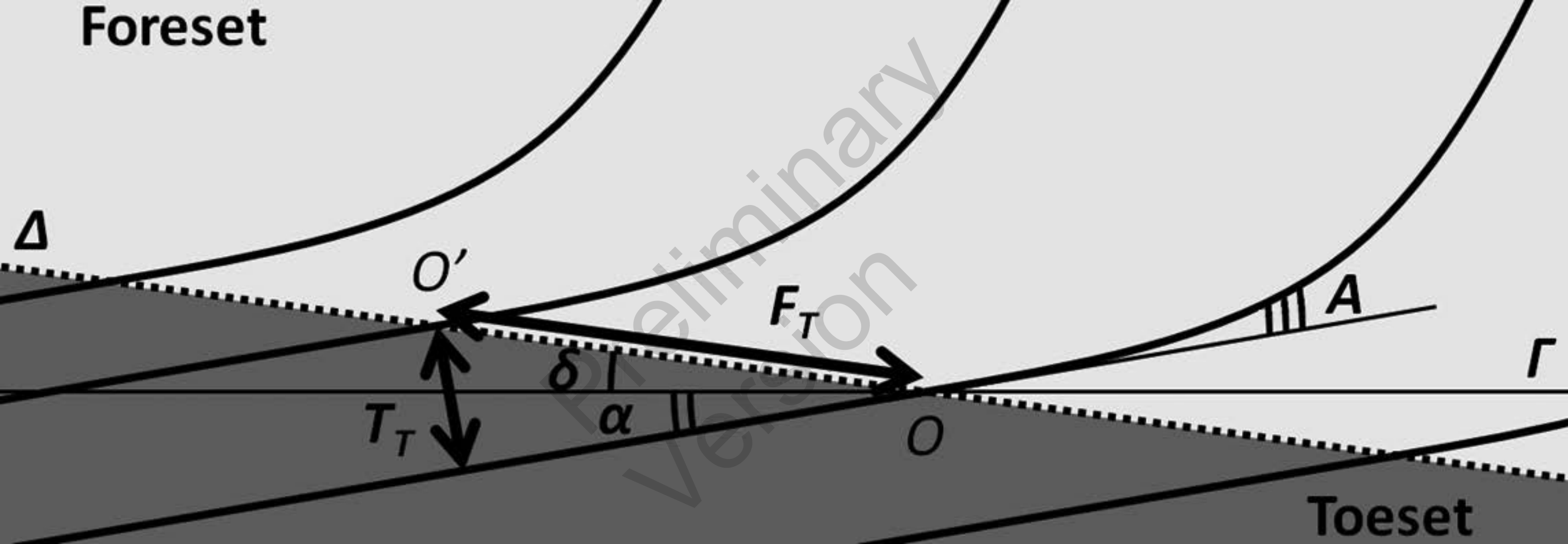


B)

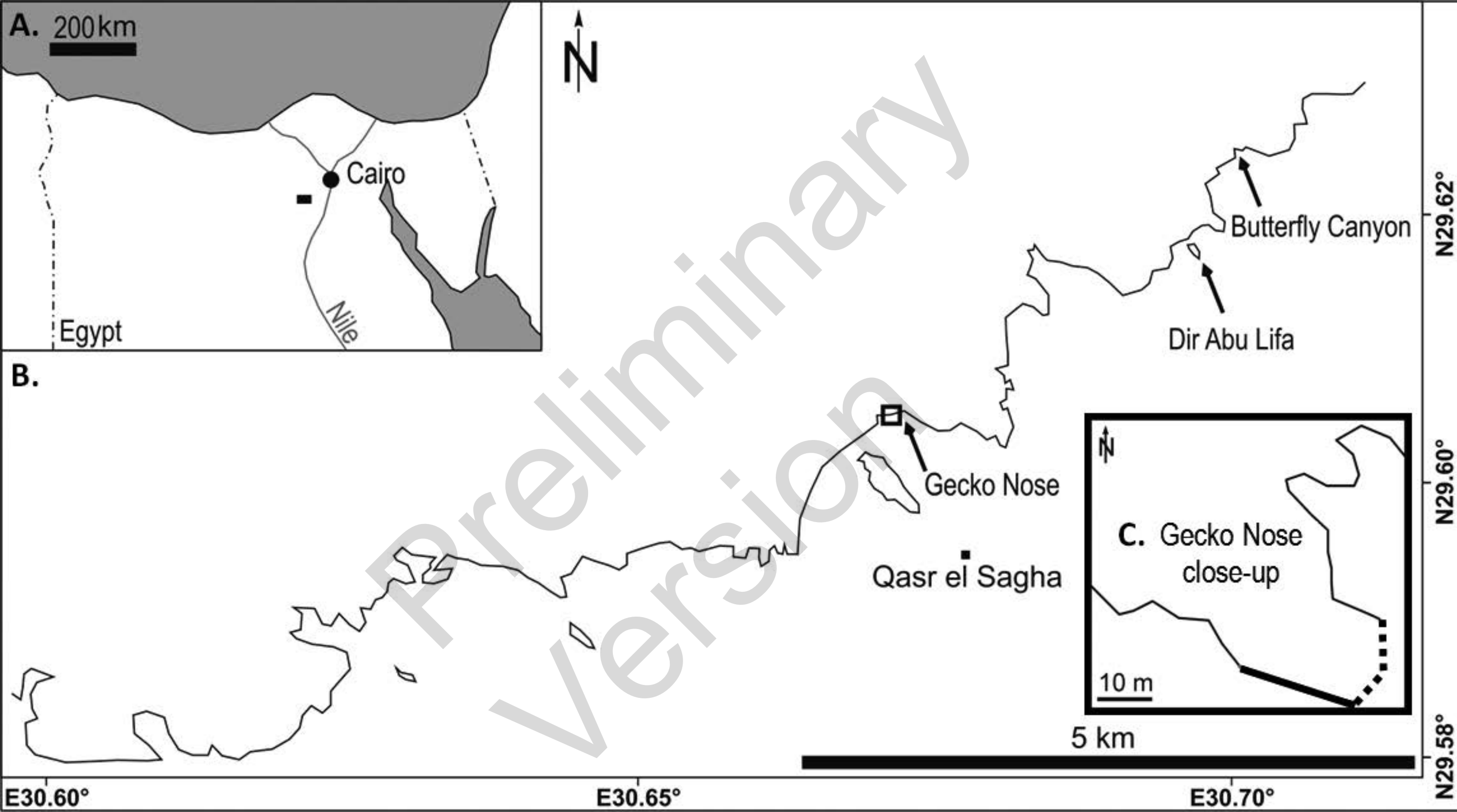


C)

Foreset



Toeset





N290
-17.0m

N110|N210
0.0

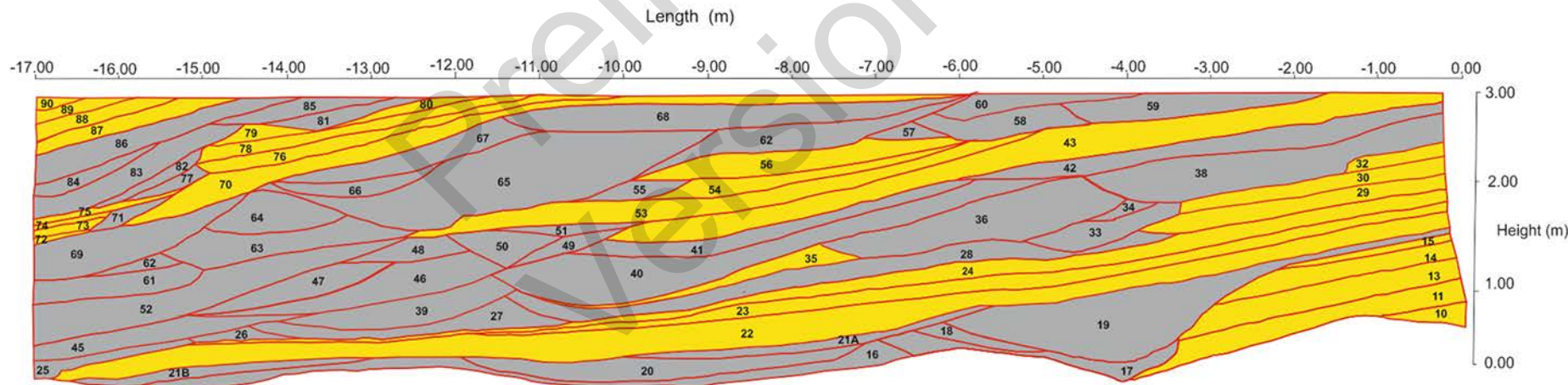
N030
12.5m

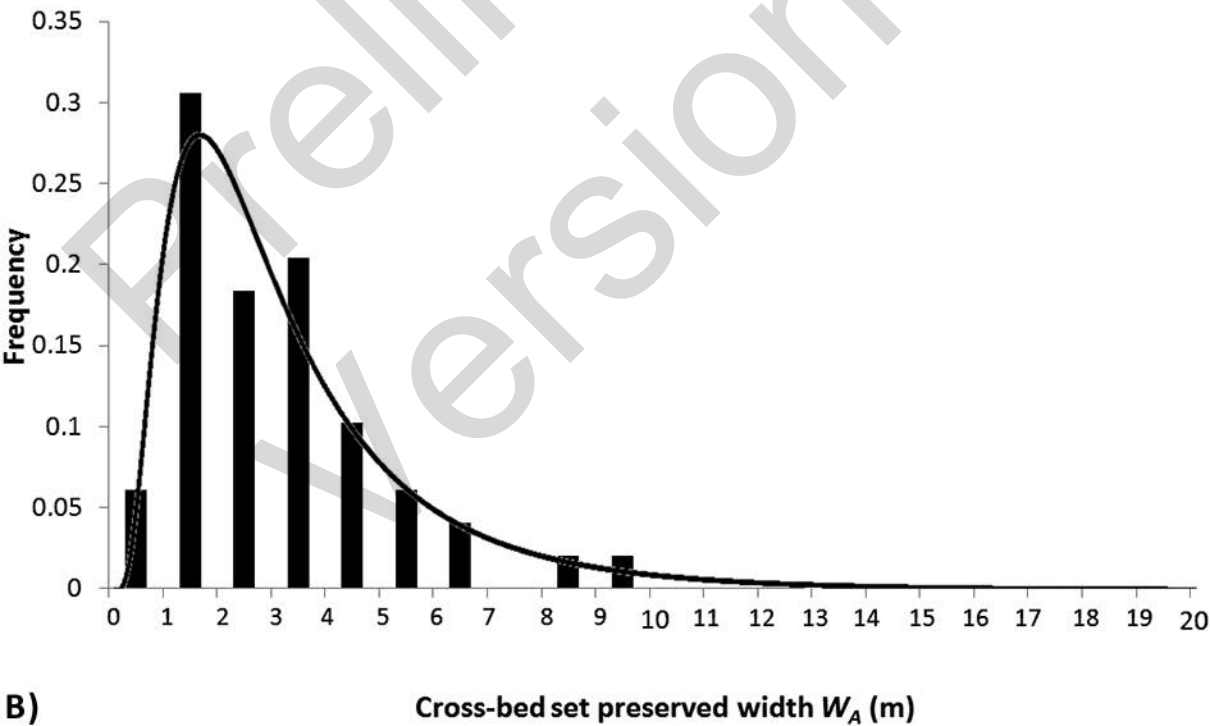
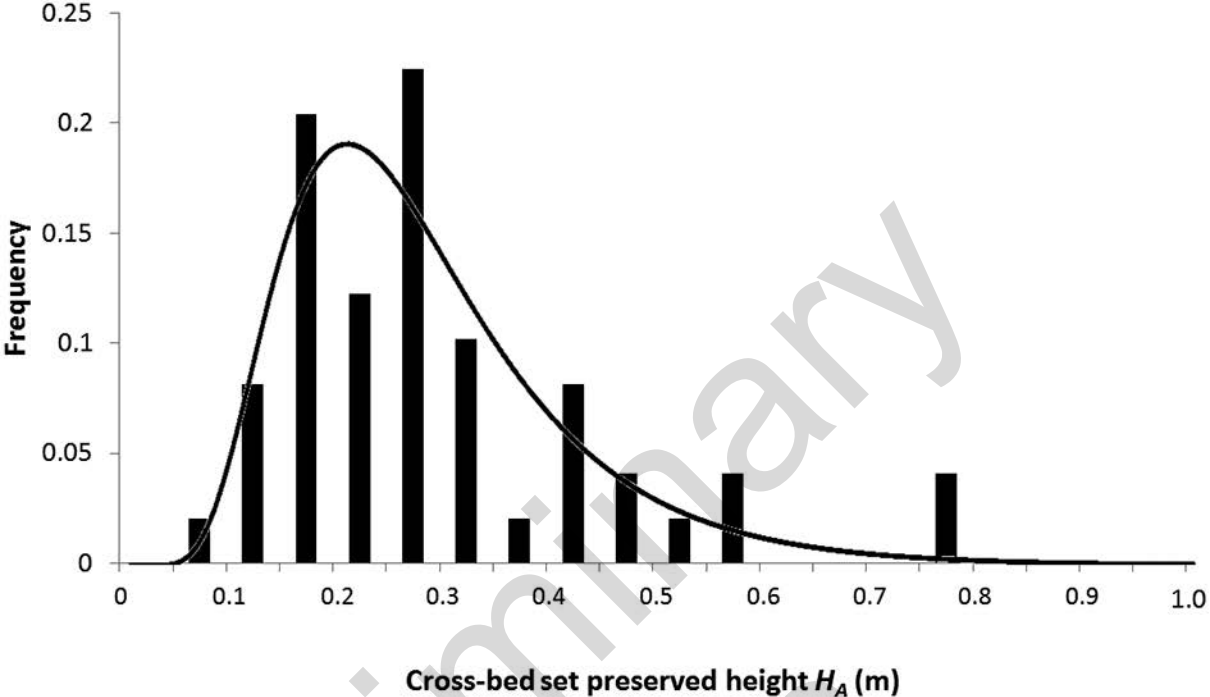
3.0m

A)

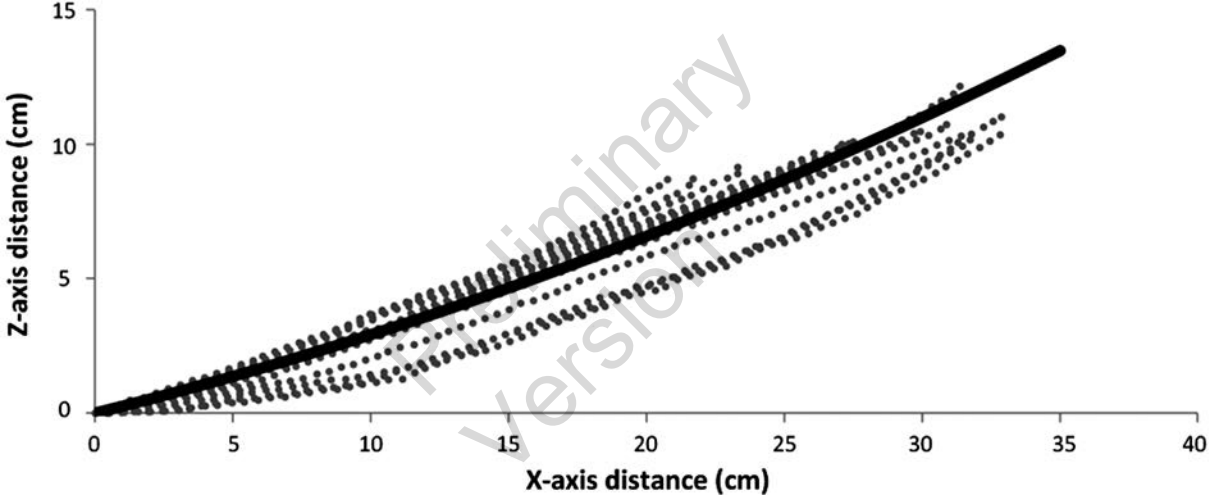


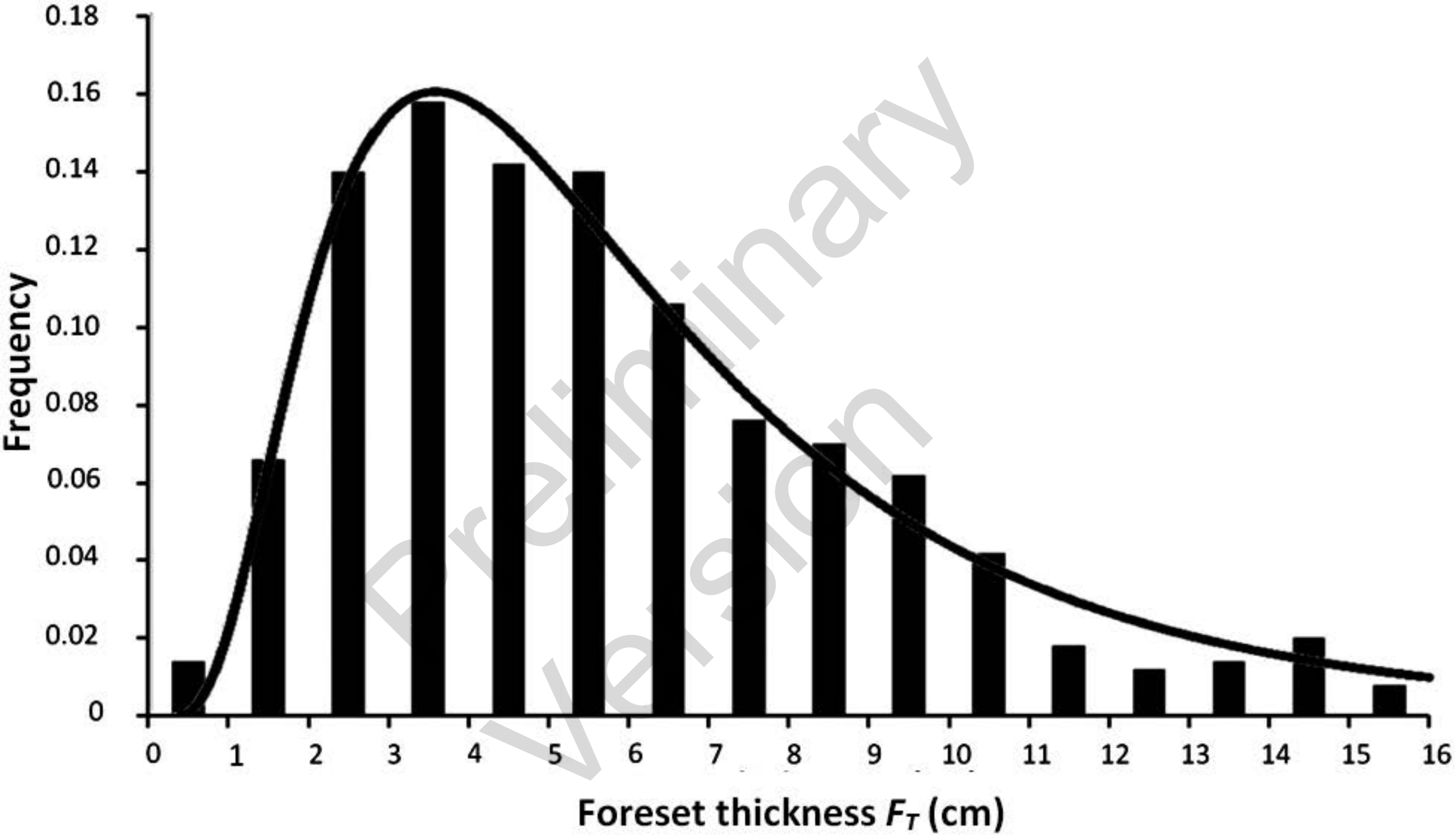
B)

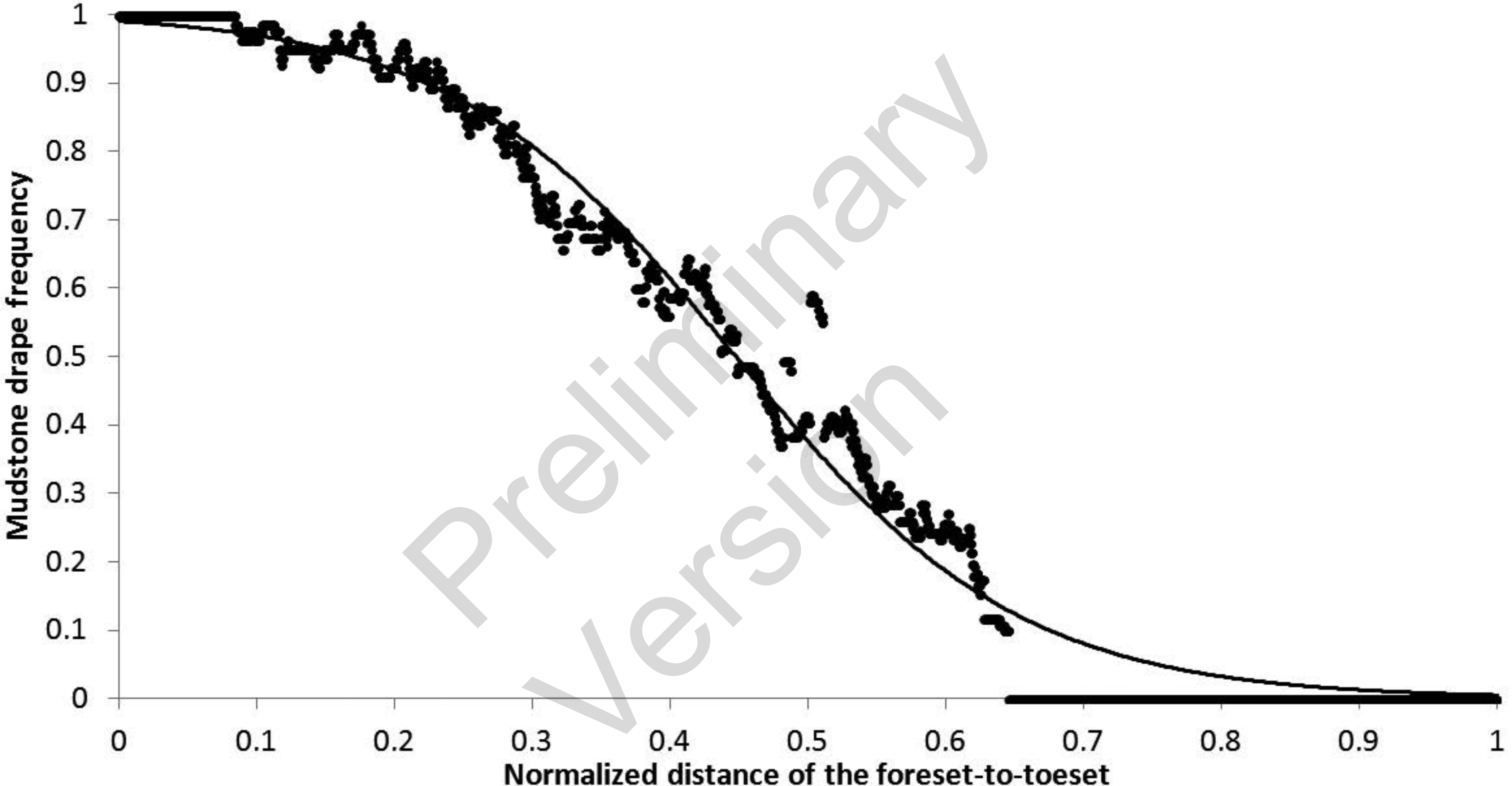




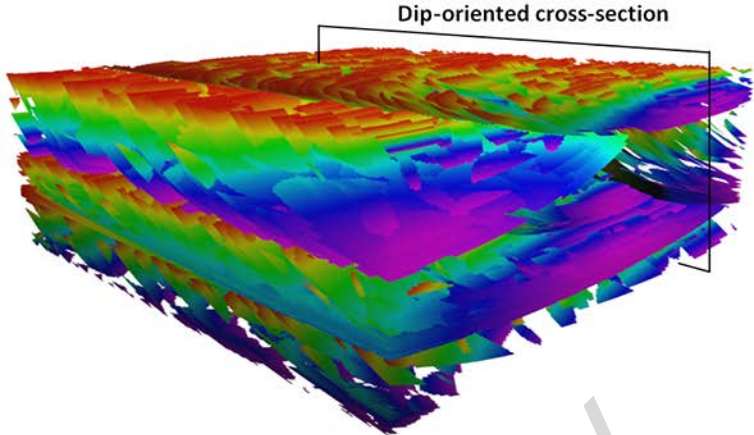
B)



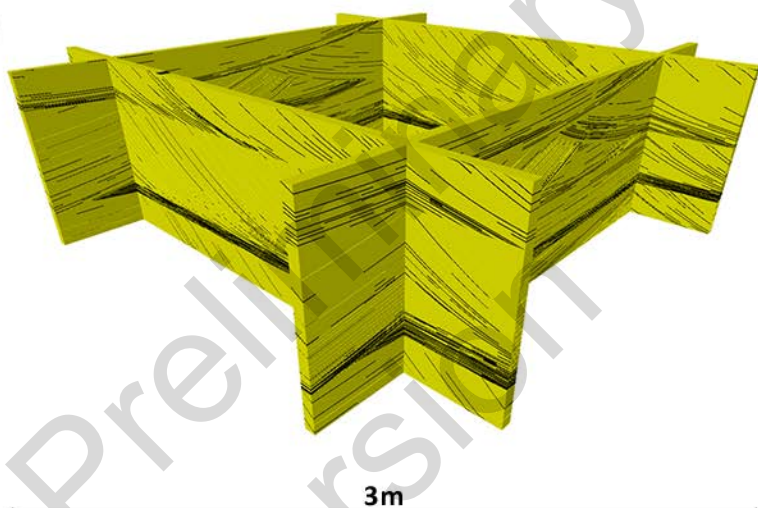




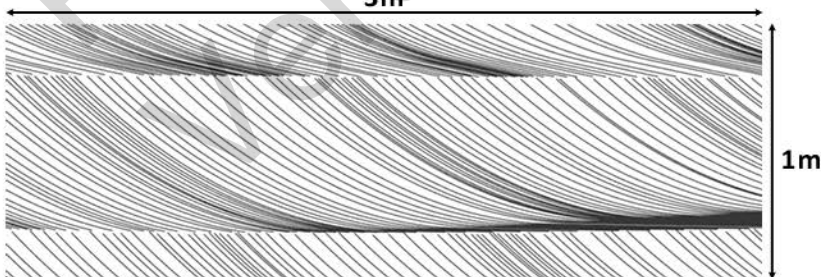
A)



B)

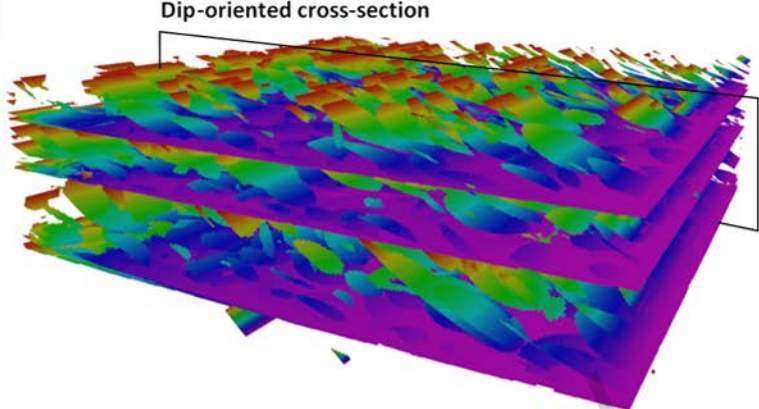
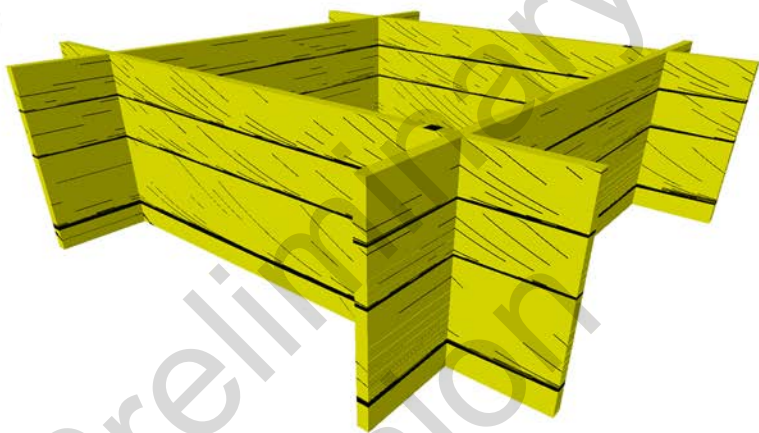
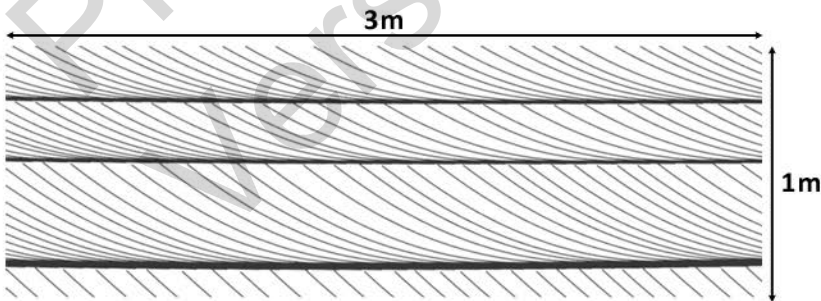
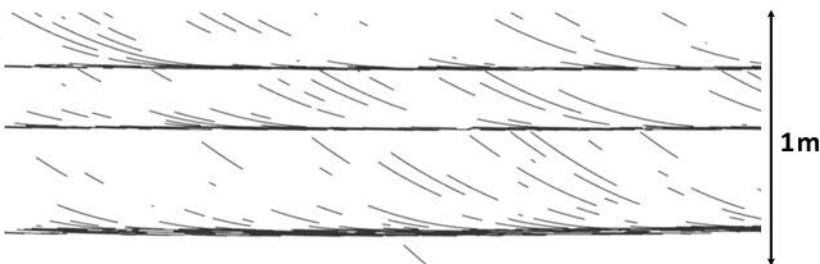


C)

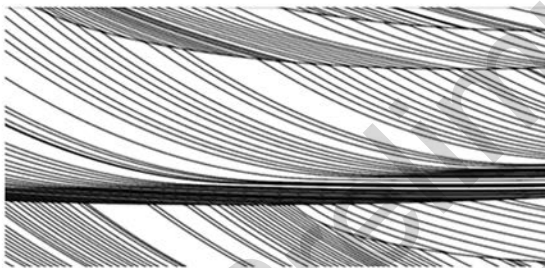
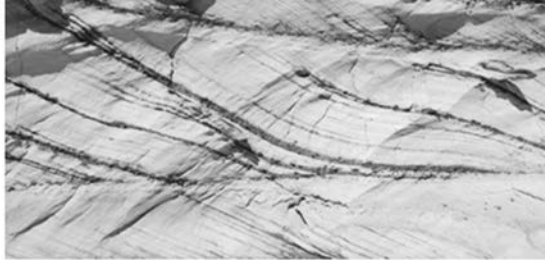


D)

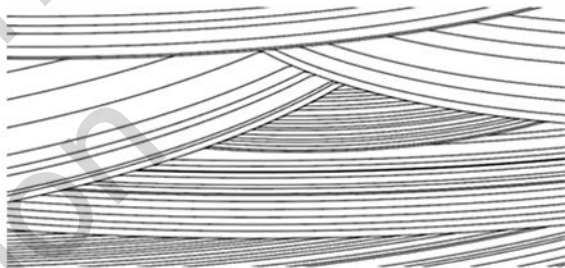
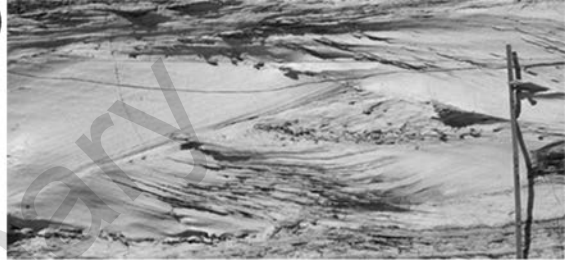


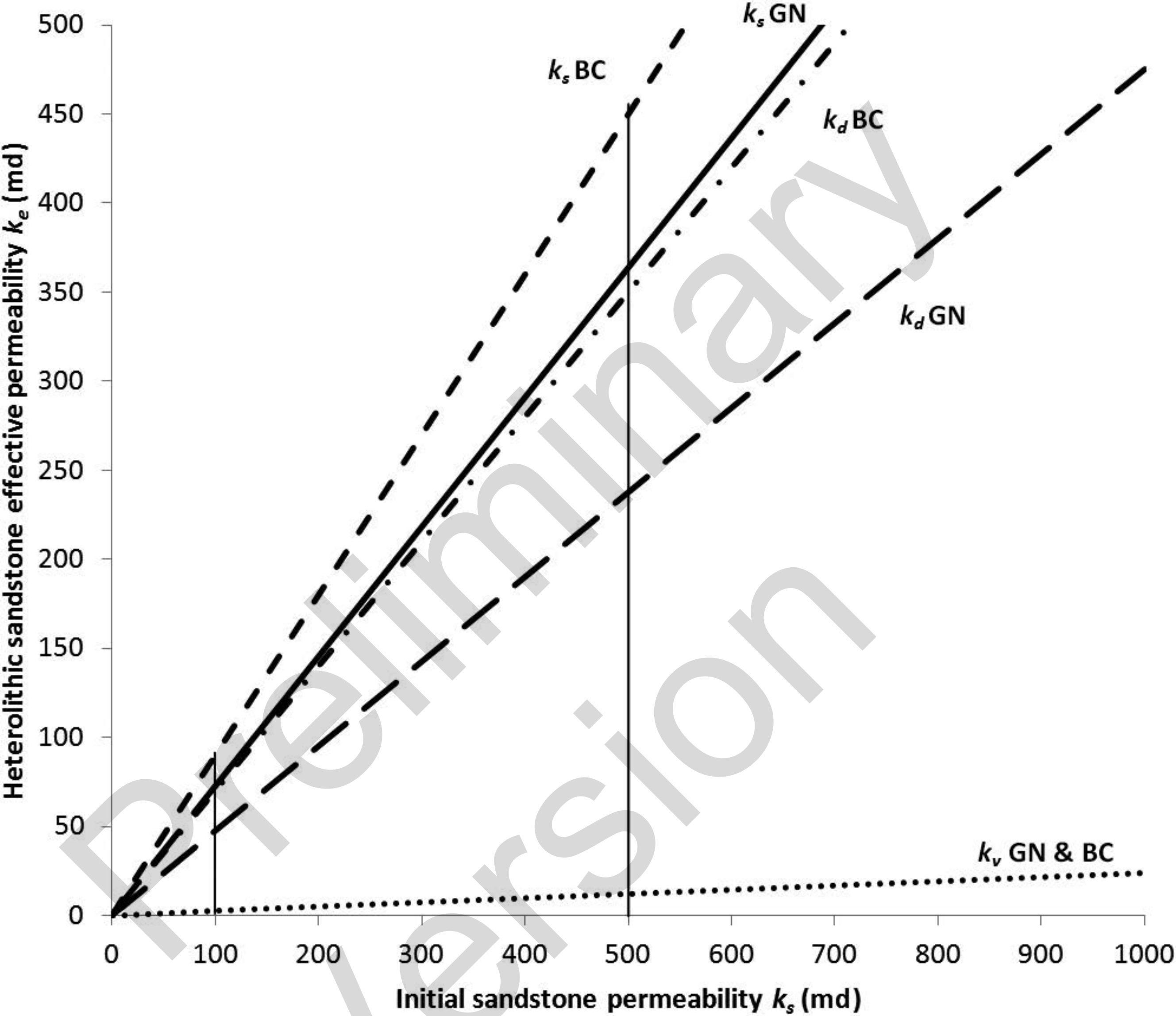
A)**B)****C)****D)**

A)



B)





Gecko Nose model

— — — k_d

————— k_s

..... k_v

Butterfly Canyon model

- . - . k_d

- - - k_s

..... k_v